Layout Synthesis of Accelerometers

Master of Science Project Report

Yong Zhou

Department of Electrical and Computer Engineering

Carnegie Mellon University

August, 1998

Committee:

Prof. Gary K. Fedder, Advisor
Dr. Tamal Mukherjee, Co-advisor

Abstract

Automatic layout generation of a surface-micromachined accelerometer from user-supplied specifications is presented. An accelerometer is an inertial sensor used to measure accelerations. An ADXL76 style accelerometer is chosen as the synthesis topology. The design problem is formulated as a formal nonlinearly constrained numerical optimization problem by using the physical dimensions of the device and sense modulation voltage as the design variables. Analytical models for both open-loop and closed-loop control are derived for the accelerometer performance characteristics in terms of the design variables. Constraints which ensure physically valid design and high-level specifications of the accelerometers, such as sensitivity, minimum detectable acceleration and maximum detectable acceleration, are defined by the using these analytical models. Objective functions such as minimize area, minimize noise, minimize a normalized sum of area and noise, and maximize range are used to drive the optimization to different parts of the design space. A generic analog force-feedback loop with phase-leading compensation is used to describe the closed-loop operation of the accelerometer. Layouts are synthesized for different objective functions. Trade-offs among different objective functions are discussed based on the generated layouts. Layouts synthesized for open-loop and closed-loop control are compared. Results show that the force-feedback control can substantially increase the range of the accelerometer.

Table of Contents

I. Introduction

With the rapid development of MicroElectroMechanical Systems (MEMS) technology, there is a demand for layout synthesis tools which can directly translate high-level design specifications into valid MEMS device layout. These synthesis tools can help designers to rapidly explore the entire design space given user-specified constraints, and assist in building complex arrayed MEMS devices by quick design of individual cells. Usually in MEMS design, designers need to decide on a certain topology, make trade-offs between performance specifications and assign values to a set of variables which can represent a valid design. Physical layout is then generated from the set of variables. Generally, the number of variables is large and finding an optimum trade-off between specifications is difficult from hand calculations.

Prior work on layout synthesis has focused on layout generation from physical definitions [1][2], requiring the user to translate the design objective into layout parameters. Also work has been done in design optimization for simple MEMS structures [3]. Recently work has been done in shape optimization for electrostatic comb drives [4]. None of those approaches obtain the entire design from device specifications automatically. A new approach has been proposed which models the design problem as a formal numerical synthesis problem, and solves it by optimization techniques [5]. A schematic of this approach is shown in Figure 1. This approach starts from a given design topology, translates the topology into design variables, determines the numerical design constraints from user specifications, geometry and manufacturing limitations. The quantitative design objective drives the optimizer to an optimum design which is then translated into a CIF layout file by the layout generator (CAMEL [1]). A folded-flexure electrostatic comb-drive-microresonator topology has been successfully used to demonstrate the ability of the synthesis approach [5].

In this report, we extend the synthesis techniques in [5] to a more complicated surface-micromachined accelerometer system. MEMS-based accelerometers have been widely used in automotive, robotics and other industries. A commonly used differential lateral accelerometer topology is used in our study. We develop a synthesis tool which not only considers the physical design of the mechanical structure of the

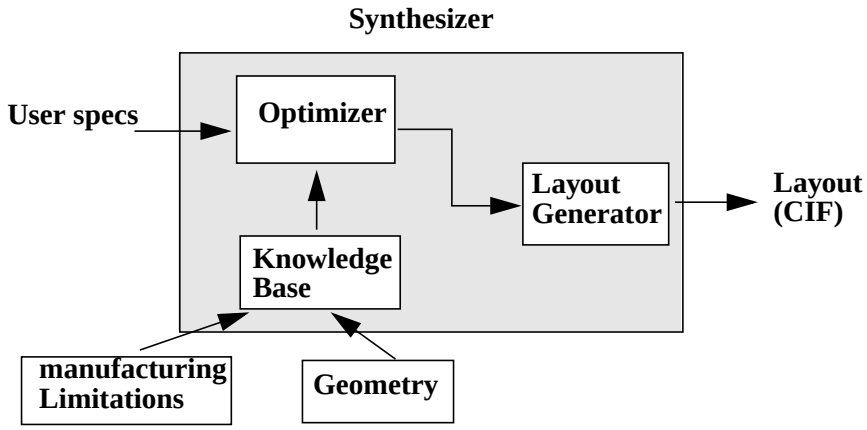

Figure 1. Schematic of layout synthesis

accelerometer, but also some design issues in the system level, for example, the interface between the mechanical structure and the sensing electronics, and the force feedback control which is used to stabilize the system and increase the maximum detectable acceleration.

Chapter 2 of this report gives an overview of the lateral accelerometer, including the topology, and its capacitive sensing scheme. In Chapter 3, lumped models and equations which describe the behavior of the accelerometer are derived. In Chapter 4, a detailed discussion of the synthesis algorithm is given. Chapter 5 gives some synthesis results and provides comparison with finite element simulations. Finally, Chapter 6 summarizes this report and suggests directions for future work.

II. Accelerometer overview

An accelerometer is an inertial sensor used to measure accelerations. Many MEMS-based accelerometers use a capacitive-sensing scheme for acceleration detection [6][12]. A simplified schematic of a capacitive accelerometer is shown in Figure 2.

The central part of the accelerometer is a suspended mechanical proof mass, which acts as the sensing element. When the accelerometer is exposed to some acceleration, the proof mass moves relative to the substrate, subject to spring restoring forces and the damping provided by the motion of air around the moving mass and comb fingers. The relative displacement is sensed by measuring the capacitance change

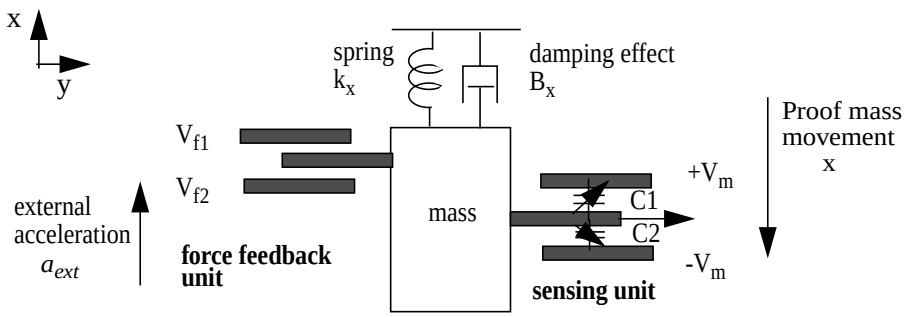

Figure 2. Schematic of an capacitive accelerometer

between the comb fingers, as shown in the sensing unit in Figure 2. During the displacement sensing, modulation voltage V_m is applied across the sense fingers. For the force feedback unit, when voltages of different amplitudes are applied across the finger gaps of the force unit, different electrostatic forces will be generated and the net force will pull the proof-mass into the desired direction. The force feedback unit may be used in closed-loop feedback control or in self test.

The performance of an accelerometer design is evaluated by specifications such as sensitivity which is defined as the ratio of output voltage over the input acceleration, minimum detectable acceleration, maximum detectable acceleration, bandwidth. Designers also need to consider geometric constraints given by manufacturing process, such as the maximum device size, the minimum beam width. A valid design must meet all the user specifications and the geometric constraints.

The layout of the capacitive accelerometer used in our synthesis is shown in Figure 3. This topology is similar to that of the ADXL150 accelerometer from Analog Devices [6].

The accelerometer consists of a movable proof-mass, suspended by two U-shape spring beams on both sides. Movable comb fingers (rotor fingers) are attached to the proof mass. They are combined with the fixed comb fingers (stator fingers) to form the sensing units and feedback force units as defined in Figure 2. At two ends of the proof mass, there are four small rectangular cantilever beams, called limit stops. They are used to limit the displacements of the proof mass in the x and y directions so that the rotor and stator fingers can not touch together. Because different voltages are applied across the finger gaps during acceler-

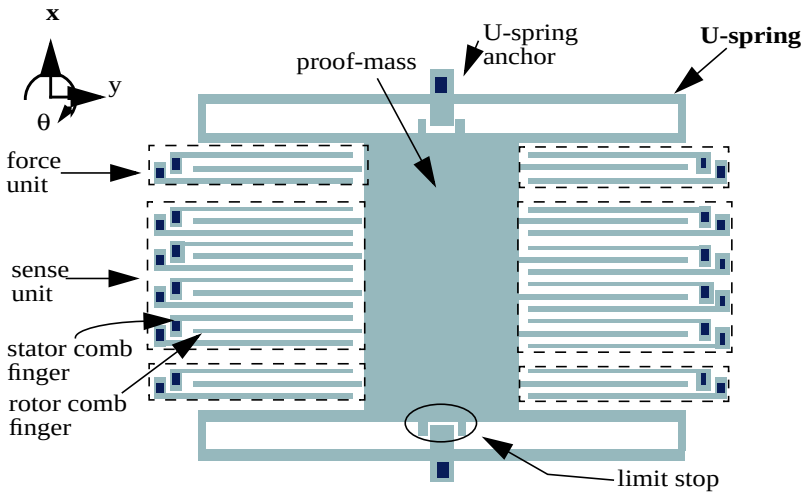

Figure 3. Layout of a lateral capacitive accelerometer

ometer operation, touch of the two fingers will cause short circuit and damage the device.

The lateral accelerometer can be fabricated by MUMPs technology from MCNC [7] or by iMEMS technology from Analog Devices [8]. In both processes, the polysilicon is used as the structural material because of its excellent mechanical properties. The conditioning circuit can either be integrated in the same chip or provided off chip.

III. Lumped parameter modeling of accelerometer

3.1. Introduction

In order to evaluate the performance of an accelerometer design, we need a set of lumped-parameter models to describe the device behavior as a function of the physical design variables. In our synthesis formulation, we model the accelerometer as a spring-mass-damper system as shown in Figure 4. The models include the effective stiffness of the spring, the effective masses of the spring and the proof mass, viscous air damping, electrostatic comb-drive force for the feedback control, and the capacitive sensing interface.

There are many specifications to evaluate the performance of the accelerometer [6]. In this report, we focus on the five most important ones: the accelerometer sensitivity, the minimum detectable acceleration

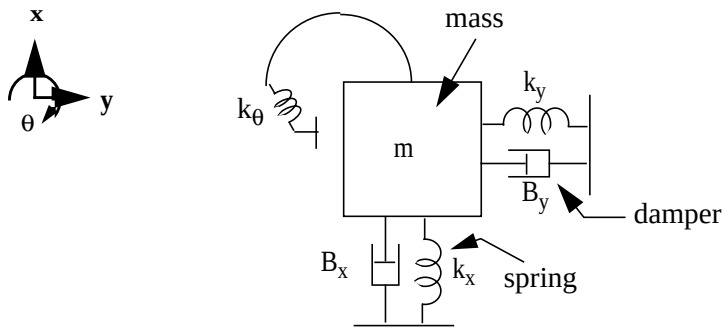

Figure 4. Spring-mass-damper model for the accelerometer

(noise), the maximum detectable acceleration (detecting range), the cross-axis sensitivity and bandwidth.

3.2. Modeling of the accelerometer system

For the mass-spring-damper system shown in Figure 4, the differential equation for the displacement x as a function of external acceleration is:

$$m_x \frac{d^2x}{dt^2} + B_x \frac{dx}{dt} + k_x x = F_{ext} = ma_{ext} \qquad (3.1)$$

where k_x is the spring stiffness, B_x is the damping coefficient, m_x is the effective mass, F_{ext} is the external force, and a_{ext} is the external acceleration.

In the following sections, we will derive analytical models of the spring constant, the effective mass, and the damping coefficient as functions of the design variables.

3.2.1 Spring stiffness models

Due to the rigidity of the proof-mass, the U-spring dominates the stiffness model. We derive the effective stiffness of the U-spring by using energy methods [9]. In this method, a force F (or moment M) is applied at the free end of the spring in the appropriate direction, and the displacement δ is found by Castigliano's second theorem. The spring constant is defined as $k = F/\delta$. This method has been used for other MEMS structures such as folded-flexure beams and crab-leg beams [10] [11].

When only displacement from bending and torsion is considered, the total strain energy U of a linear

structure is calculated as

$$U = \sum_{i=1}^{N} \int_0^{L_i} \frac{M_i(\xi)^2}{2EI_i} d\xi \tag{3.2}$$

where E is the Young's modulus of the material, L_i is the length of the i'th beam in the spring, $M_i(\xi)$ is the bending moment along the beam i, and ξ is the distance from the beam end. The bending moment M_i is calculated from the forces and the moments applied at the end point of the spring.

From Castigliano's second theorem, the partial derivative of the strain energy U with respect to a given force F_j is equal to the displacement at the force point, δ_j.

$$\delta_j = \frac{\partial U}{\partial F_j} \tag{3.3}$$

Similarly, the angular displacements, θ_j, resulted from applied moments, M_j is given by:

$$\theta_j = \frac{\partial U}{\partial M_j} \tag{3.4}$$

According to the direction of interest, different boundary conditions are applied to the beam ends, resulting in a set of simultaneous equations. The analytic relation of the displacement and the applied force can be obtained by solving those equations.

Using the method described above, we derive the U-spring stiffness. A schematic of the U-spring suspension is shown in Figure 5.

In the x-direction, a force F_x is applied at the free end point A. From symmetry considerations when used in the accelerometer, the boundary conditions $\delta_y = 0$ and $\delta_\theta = 0$ are obtained. Solving the simultaneous equations from the energy method, the x-direction spring stiffness for the simplified case $L_{b1} = L_{b2} = L_b$ and $W_{b1} = W_{b2} = W_b$ is:

$$k_x = \frac{12\alpha EI_b}{L_t^2(6\alpha L_b + L_t)} \tag{3.5}$$

where E is the Young's modulus of polysilicon, L_b and L_t are the lengths of beams and truss, W_t and W_b are

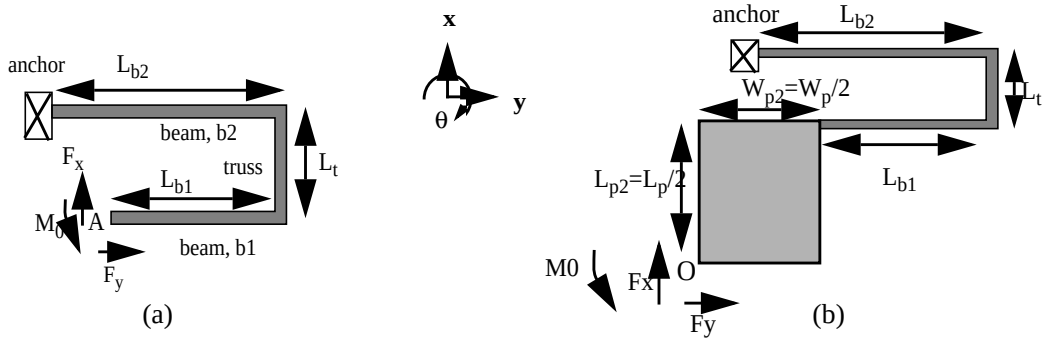

Figure 5. Schematic of U-spring for spring stiffness calculation. (a) forces and moments applied on the U-spring beams for k_x and $k_y$calculation. (b) U-spring and a quarter of proof mass for k_θ calculation.

the beam and truss widths, I_b is the bending moment of inertia of beam b1 and b2, $I_b = tW_b^3/12$, $\alpha = (W_t/W_b)^3$. From equation (3.5) we can see that k_x is getting smaller when L_t or L_b increases.

Similarly, when a y-direction force F_y is applied, we have the boundary conditions $\delta_x = 0$ and $\delta_\theta = 0$. The y-direction stiffness for the simplified case $L_{b1} = L_{b2} = L_b$ and $W_{b1} = W_{b2} = W_b$ is:

$$k_y = \frac{3EI_b(2\alpha L_b + Lt)}{L_b^3(\alpha L_b + 2L_t)} \qquad (3.6)$$

The calculation of torsional spring constant in the θ direction, k_θ (the rotation-about-z mode), is a little different from that of k_x and k_y. The schematic for k_θ calculation is shown in Figure 5(b). Instead of applying the boundary condition at the beam end of the U-spring, we apply the boundary condition $\delta_x = 0$ and $\delta_y = 0$ at the center of proof mass, point O, when a moment M_0 is applied, because we can not rotate the beam end about the z direction and keep δ_x and δ_y of the beam end to be zero.

The full expression for calculated k_θ is very long and is not listed here. For the simplified case $W_t = W_b$, $L_{b1} = L_{b2} = L_b$ and $L_b \gg L_t$, k_θ is:

$$k_\theta = \frac{EI_b[12L_{p2}^2L_b^2 + 12L_{p2}L_tL_b^2 + L_t^2(36L_bW_{p2} + 36W_{p2}^2 + 15L_b^2)]}{6L_b^3L_t^2} \qquad (3.7)$$

where I_b is the moment of inertia of both beam and truss, and L_{p2} and W_{p2} are half of the proof-mass length and width, respectively, as shown in Figure 5(b).

3.2.2 Effective mass models

The effect of spring mass on resonant frequency of different modes is taken into account by an effective mass model. Effective mass for each mode of interest is calculated by normalizing the total maximum kinetic energy of the spring by the maximum proof-mass velocity, v_{max},

$$m_{eff} = \sum_{i}^{N} \frac{m_i}{L_i} \int_0^{L_i} \left(\frac{v_i(\xi)}{v_{max}} \right)^2 d\xi \qquad (3.8)$$

where m_i and L_i are the mass and the length of the i'th beam in the spring. Analytic expressions for the velocities, v_i, along the spring beams are approximated from static mode shapes of the U-spring deflection.

The effective mass of the movable part of the accelerometer in the x-direction is

$$m_x = m_{pr} + 4m_{sp,\,x} \qquad (3.9)$$

where m_{pr} is the total mass of the proof mass and the movable fingers, and $m_{sp,x}$ is the effective mass of the U-spring in x-direction. The full equation $m_{sp,x}$ by using equation (3.8) in general case is very long. For $W_t = W_b = W$ and $L_{b1} = L_{b2} = L_b$,

$$m_{sp,\,x} = \frac{\rho t W \left(192L_b^5 + 864L_b^4 L_t + 1112L_b^3 L_t^2 + 280L_b^2 L_t^3 + 21L_t^5 \right)}{280L_b^2 (L_b + 2L_t)^2} \qquad (3.10)$$

where ρ is the density of the polysilicon, t is the thickness of polysilicon.

The effective mass in y-direction is same as equation (3.9), but have the spring effective mass in y-direction $m_{sp,y}$ instead of $m_{sp,x}$. Also for the simplified case, $W_t = W_b = W$ and $L_{b1} = L_{b2} = L_b$,

$$m_{sp,\,y} = \frac{\rho t W \left(966L_b^5 + 315L_b^4 L_t + 164L_b^2 L_t^3 + 87L_b L_t^4 + 13L_t^5 \right)}{1260L_b^4} \qquad (3.11)$$

The moment of inertia about the z axis, I_θ is calculated assuming the entire structure rotates by same angle [11],

$$I_\theta = \sum_{rectangular, i=1}^{N} \left(m_i \frac{W_i^2 + L_i^2}{12} + m_i r_i^2 \right) \tag{3.12}$$

where m_i is the mass of the i'th rectangular block, W_i and L_i are the width and length, and r_i is the distance of the center of mass of the rectangular block from center of rotation. The result calculated from this formula is over estimated because beam rectangular blocks closer to the anchor point do not rotate as much as the proof mass.

3.2.3 Air damping model

The damping of the accelerometer comes from both structural damping and viscous flow of air around the structural region [12]. Since the amplitude of air damping at atmospheric pressure is orders of magnitude higher than the structural damping, the latter is ignored [12]. The air damping of the accelerometers topology can be classified into Couette-flow damping below the accelerometer, Stokes flow above the accelerometer, and the squeeze-film damping between the comb fingers. Couette-flow damping is due to the shear flow of air between parallel plates. For example, the air flow between the proof mass and the substrate during the proof mass motion. The viscous damping coefficient of Couette flow can be modeled by

$$B_{Couette} = \frac{\mu}{d_f} A \tag{3.13}$$

where μ is the viscosity of air, d_f is the air film thickness and A is the plate area.

The motion of the fluid above the top surface of the plate can be modeled as Stokes flow [13], in which the amplitude of fluid oscillation decays exponentially with distance from the plate surface. Let δ be the penetration depth, the damping coefficient of Stokes flow is

$$B_{Stokes} = \frac{\mu}{\delta} A \tag{3.14}$$

Squeeze-film damping occurs when the air gap between two closely placed parallel surfaces changes. For the lateral accelerometer, the squeeze film damping between comb fingers when the accelerometer

moves in x-direction changes to Hagen-Poiseuille flow because the narrow air gap width. In this case, edge effects represent a significant percentage of the total damping [12]. The damping coefficient of Hagen-Poiseuille flow between a single comb finger is given by:

$$B_{Hagen} = 7.2\mu l\left(\frac{t}{g}\right)^3 \tag{3.15}$$

where μ is the viscosity of air, l is the finger length, t is the finger thickness, and the g is the air gap between two fingers.

So the total damping coefficient is

$$B = \mu(A_{pm} + 0.5A_t + 0.5A_b)\left(\frac{1}{d_f} + \frac{1}{\delta}\right) + N_f 7.2\mu l\left(\frac{t}{g}\right)^3 \tag{3.16}$$

where A_{pm}, A_t, A_b are the areas of the proof mass and comb fingers, spring truss, and beam respectively. Here we assume the trusses and beams travel at half the velocity of the proof mass on average [14]. More accurate estimate can be found by shape approximation discussed in Section 3.2.2. N_f is total number of the comb fingers.

In practical designs, etch holes are usually added to the proof mass to ensure the structure is completely released. The etch holes can reduce damping by several orders of magnitude [15] which we do not consider in our present synthesis. To obtain accurate predictions of damping with etch holes, the proof mass should be broken into a collection of smaller plates acting in parallel [16]. The total damping is the sum of damping from each of the individual plates.

3.2.4 Electrostatic drive force model

In the force feedback units shown in Figure 2, electrostatic force is used for force-balance feedback or self-test. Assuming no fringe-field effects the electrostatic force for the single comb finger gap is:

$$F_{elec} = \frac{d}{dg_f}\frac{C_F V_{dr}^2}{2} = \frac{C_F}{2g_f}V_{dr}^2 \tag{3.17}$$

where V_{dr} is the drive voltage, g_f is the force comb-finger gap and $C_F = \varepsilon A/g_f$ is the capacitance

between force comb fingers. From equation (3.17) we can see that, the electrostatic force has quadratic dependence on the drive voltage which is not desired for analog force control. A simple solution for linearization of the electrostatic force is to apply voltages $V_{c,dr}+V_{dr}$ and $V_{c,dr}-V_{dr}$ separately across the two comb finger gaps [17]. Here $V_{c,dr}$ is a fixed center voltage and V_{dr} is the controlling drive voltage. The two resulting forces are in the opposite directions and the quadratic terms cancel. This results in a net force

$$F = \frac{2V_{c,dr}V_{dr}C_F}{g_f} \tag{3.18}$$

which linearly depends on the controlling voltage V_{dr}.

3.2.5 Electrostatic spring softening model

In the sense units shown in Figure 2, when the modulation voltage, V_m, is applied between the sensing fingers, electrostatic forces are generated on the proof mass as shown in Figure 6. It will change the actual effective spring constant of the system from its mechanical value.

The net force applied to a single finger is

$$F = \frac{\varepsilon A V_m^2}{2(g_0 - x)^2} - \frac{\varepsilon A V_m^2}{2(g_0 + x)^2} = \frac{C_0 V_m^2 g_0}{2}\left(\frac{1}{(g_0 - x)^2} - \frac{1}{(g_0 + x)^2}\right) \tag{3.19}$$

where g_0 is the initial gap between the fingers, $A = l_{overlap}t_{finger}$ is the area of the finger sidewall, and $C_0 = \varepsilon A / g_0$ is the initial capacitance between the fingers when $x = 0$. The effective electrostatic spring

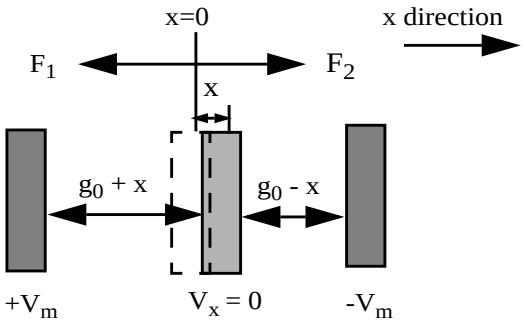

Figure 6. Electrostatic spring model

constant is obtained by differentiating equation (3.19), for $x \ll g_0$,

$$k_e = -\frac{\partial}{\partial x}(F) = -\frac{2C_0V_m^2}{g_0^2} = -\frac{2\varepsilon AV_m}{g_0^3} \tag{3.20}$$

The electrostatic force is in the opposite direction of the mechanical spring force, so the actual effective spring constant is $k_{eff} = k_{mech} + k_e$.

3.3 Accelerometer performance evaluation models in open-loop operation

The accelerometer can either be operated open loop or closed loop. In closed-loop operation, the displacement of the proof mass due to an applied acceleration is sensed and a restoring force is generated to counteract the motion. The open-loop accelerometer system is simple to design and is cost efficient. We will first derive the equations that models the accelerometer performance in open-loop operation. The models for closed-loop operation will be discussed in Section 3.4.

3.3.1 Accelerometer sensitivity

The sensitivity of the accelerometer is defined as the ratio of output voltage over the input acceleration. It is determined by both the mechanical design of the sensor and the position sense circuit. We first need to find the mechanical sensitivity which is defined as how much the proof mass moves when an acceleration is applied.

We use the Laplace transform to solve the second-order system given by equation (3.1):

$$\frac{X(s)}{A(s)} = \frac{m}{m_x s^2 + B_x s + k_x} = \frac{1}{s^2 + s\frac{\omega_r}{Q} + \omega_r^2} \tag{3.21}$$

where $\omega_r = \sqrt{k_x/m}$ is the resonant frequency and $Q = \omega_r m/B$ is the quality factor. At frequencies well below resonance ($\omega \ll \omega_r$), the mechanical sensitivity is

$$\frac{x}{a} = \frac{1}{\omega_r^2} = \frac{m_x}{k_x} \tag{3.22}$$

From equation (3.22) we can see that the mechanical sensitivity is inversely proportional to the square of the resonant frequency. To achieve high sensitivity, the resonant frequency should be made low. In practice, there is a limit for ω_r because of the mechanical shock resistance and the manufacturability.

We choose a commonly used single-ended half-bridge capacitive sense interface to translate the proof mass displacement into output voltage, as shown in Figure 7, because this scheme is easy to implement in both the MUMPS and the iMEMS processes.

In Figure 7, C_1 and C_2 are capacitors between the movable finger and its nearest fixed finger. The modulation voltages V_m are applied between those fingers. The modulation voltages are usually operated at high frequency to suppress offset and flicker noise [17]. C_{para} is the total parasitic capacitance at the output V_o node, including the parasitic capacitance from proof mass to substrate, parasitic capacitance due to anchors and the parasitic from the signal conditioning circuits.

Applying Kirchhoff's current law at node V_o in Figure 7 yields:

$$V_o = \frac{C_1 - C_2}{C_1 + C_2 + C_{para}} V_m \qquad (3.23)$$

When no acceleration occurs, the movable finger is midway between the two fixed sense fingers, $C_1 = C_2 = C_0$, and the output voltage V_o is zero. Under an applied acceleration, the proof mass moves a displace-

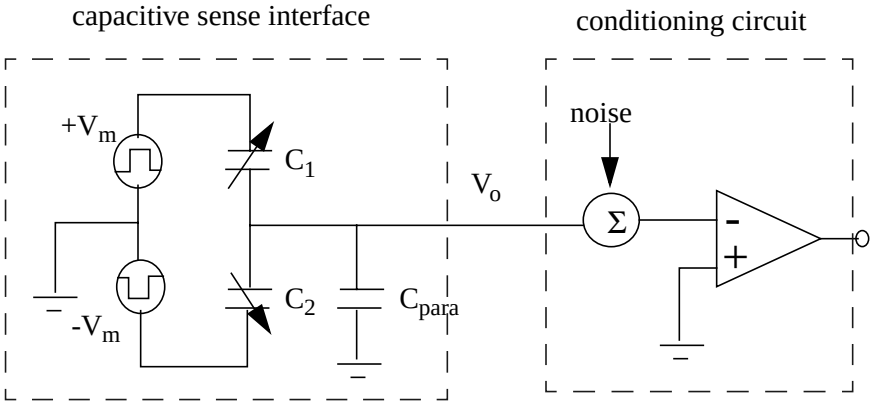

Figure 7. Accelerometer sensing interface

ment x governed by equation (3.22) and C_1 and C_2 are no longer equal. We use a parallel-plate model to approximate the capacitance and assume the displacement x is small compared to the initial gap g_0:

$$C_1 = \varepsilon_0 \frac{A}{(g_0 - x)} \approx \varepsilon_0 \frac{A}{g_0}\left(1 + \frac{x}{g_0}\right) = C_0\left(1 + \frac{x}{g_0}\right) \tag{3.24.a}$$

$$C_2 = \varepsilon_0 \frac{A}{(g_0 + x)} \approx \varepsilon_0 \frac{A}{g_0}\left(1 - \frac{x}{g_0}\right) = C_0\left(1 - \frac{x}{g_0}\right) \tag{3.24.b}$$

combine equation (3.23) and (3.24), we have

$$V_0 = \left(\frac{2C_0}{2C_0 + C_{para}} \frac{x}{g_0}\right) V_m = \frac{2C_0}{2C_0 + C_{para}} \frac{ma}{kg_0} V_m \tag{3.25}$$

and the sensitivity is

$$\frac{V_0}{a} = \frac{2C_0}{2C_0 + C_{para}} \frac{m}{kg_0} V_m \tag{3.26}$$

The sensitivity is inversely proportional to the initial gap between the sensing fingers. Also the parasitic capacitance should be minimized to obtain high sensitivity. Note that the sensitivity we derived here only includes the mechanical structure and the capacitive sense interface. The output voltage V_o usually will be further amplified by later conditioning circuits [6][12].

3.3.2 Minimum detectable acceleration

The minimum detectable acceleration is determined by the total noise referred back to the accelerometer input. In our synthesis, we consider two noise sources. One is the Brownian (thermal) noise in the mechanical domain which comes from the random collision of the air molecules with the accelerometer. The second noise source is transistor noise in the front-end circuit.

For a damped suspended proof mass, the Brownian equivalent acceleration is [17]:

$$\sqrt{\overline{a^2_{n-Brownain}}} = \frac{\sqrt{4k_B TB}}{m}\sqrt{\Delta f} = \sqrt{\frac{4k_B T\omega_r}{mQ}}\sqrt{\Delta f} \tag{3.27}$$

where k_B is Boltzman's constant, T is the temperature, B is the damping factor and Q is the quality factor.

Let $V_{n\text{-}circuit}$ be the noise coming from the electrical circuit. We refer this noise into the input acceleration:

$$a_{n-circuit} = \frac{V_{n-circuit}}{sensitivity} \tag{3.28}$$

The minimum detectable acceleration equals to the total input acceleration noise:

$$a_{min} = \sqrt{a_{n-circuit}^2 + \overline{a_{n-Brownain}^2}} \tag{3.29}$$

3.3.3. Maximum detectable acceleration

In the operation of the accelerometer, a large input will cause the proof mass to hit the limit stop. The maximum detectable acceleration is defined as the largest acceleration the system can detect before hitting the limit stop. When the accelerometer operates in open loop and an acceleration is applied, in steady state, the proof-mass is subjected to an inertial force, a mechanical spring force and an electrical spring force as discussed in Section 3.2.5. With the increase of the acceleration, the mechanical restoring force may not be able to match the sum of inertial force and the electrical spring force at some point, and the proof mass will snap into the limit stop. At equilibrium, the mechanical force equals to the sum of inertial force and the electrical force.

$$k_x x = m_x a + \frac{C_0 V_m^2 g_0}{2}\left(\frac{1}{(g_0 - x)^2} - \frac{1}{(g_0 + x)^2}\right) \tag{3.30}$$

where x is the displacement of the proof-mass and g_0 is the initial gap between sense fingers.

Let $E_0 = C_0 V_m^2 / 2$, the equilibrium acceleration which satisfies equation (3.30) is a function of x:

$$a_{eq}(x) = \frac{kx(g_0^2 - x^2)^2 - 4E_0 g_0^2 x}{m(g_0^2 - x^2)^2} \tag{3.31}$$

A schematic diagram of $a_{eq}(x)$ vs. x is shown in Figure 8.

Differentiating equation with respect to *x* and set the result to zero, *a(x)* is found to have a maximum at:

$$x_{snap} = g_0\sqrt{1-\frac{2E_0}{D}+\frac{2D}{kg_0^2}} \qquad D = \left(-E_0 g_0^4 k^2 + E_0 g_0^3 k^{3/2}\sqrt{E_0 + g_0^2 k}\right)^{1/3} \tag{3.32}$$

The snap-in acceleration a_{snap} is found by substituting x_{snap} into equation (3.31):

$$a_{snap} = \frac{kg_0}{m}R\left(1-\frac{4E_0}{kg_0^2(1-R^2)^2}\right) \tag{3.33}$$

where $R = \sqrt{1-2E_0/D+2D/(kg_0^2)}$.

For accelerations smaller than a_{snap}, the proof mass is in stable equilibrium and x increases with input acceleration. When accelerations are larger than a_{snap}, the gap is reduced to less than $g_0 - x_{snap}$ and the increase of the mechanical restoring force is slower than the increase of electrostatic force, snap-in will occur. The proof mass is in unstable equilibrium for this case. If the gap between the proof mass and the limit stop x_{limit} is larger that x_{snap}, the maximum detectable acceleration a_{max} in open-loop is a_{snap}. Otherwise, a_{max} is a_{limit} as shown in Figure 8 which can be found by set $x = x_{limit}$ in equation (3.31)

$$a_{limit} = \frac{kg_0}{m}R'\left(1-\frac{4E_0}{kg_0^2(1-R'^2)^2}\right) \tag{3.34}$$

where $R' = x_{limit}/g_0$.

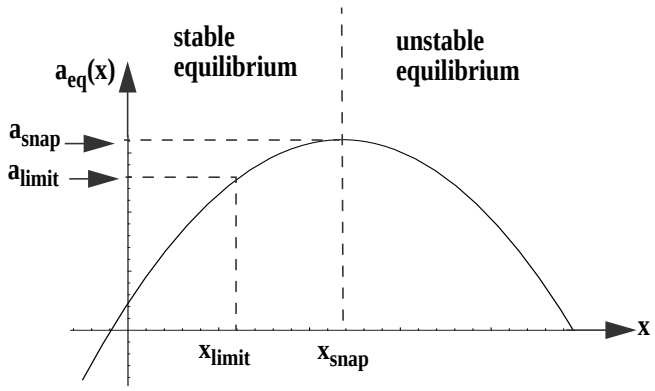

Figure 8. Schematic diagram for snap-in acceleration calculation

3.3.4 Cross-axis sensitivity

Cross-axis sensitivity occurs when the primary axis output voltage is created by forces in the orthogonal axis. In our design, the primary axis is the x-axis. Cross-axis sensitivity can come from the misalignment of the package orientation [6] or come from process variations, for example, the mismatch in the etch wall of the spring beam and truss [18]. In our synthesis, we only consider the process variations since the misalignment of package is beyond the scope of layout synthesis.

The capacitive sensing units are connected in such a way that the top stator fingers are at the same potential and so are the bottom stator fingers, as shown in Figure 9. Note here we have $C_1 = C_{11} + C_{12}$ and $C_2 = C_{21} + C_{22}$, where C_1 and C_2 are the half-bridge capacitors shown in Figure 7. When there is a displacement in y-direction, C_{11} and C_{21} will be decreased by ΔC, and C_{12} and C_{22} will be increased by ΔC. For the half-bridge sense circuit shown in Figure 7, there is zero output voltage because $C_1 = C_2$. The displacement in z direction will cause C_{11}, C_{21}, C_{12} and C_{22} to change by the same amount, there is also a zero output voltage. A non-zero voltage output can be produced only when there is displacement in the primary x direction.

When a y-directed force is applied to the proof mass, displacement in x-direction is determined by the compliance coefficient α_{xy} in the 3-DOF (degree of freedom) compliance matrix of the U-spring suspen-

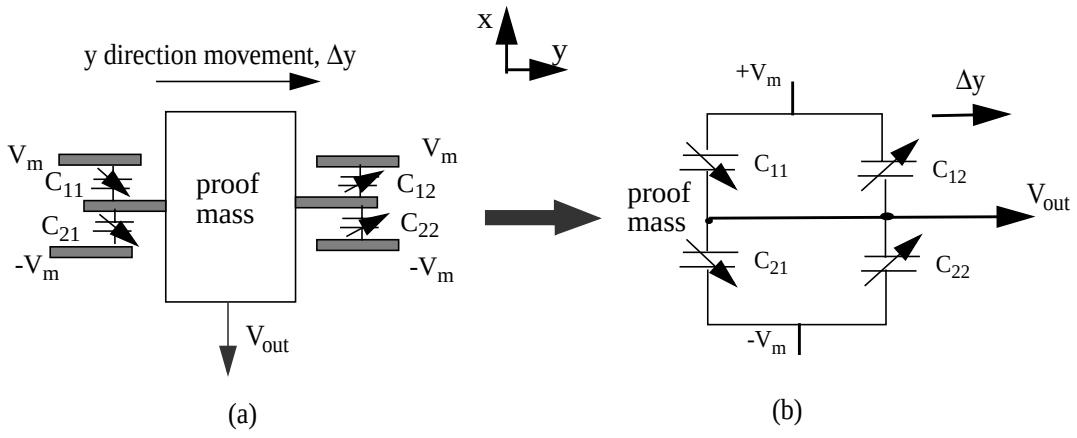

Figure 9. Sense capacitor behavior during y-directed motion

sion:

$$\begin{bmatrix} x \\ y \\ \theta \end{bmatrix} = \begin{bmatrix} \alpha_{xx} & \alpha_{xy} & \alpha_{x\theta} \\ \alpha_{yx} & \alpha_{yy} & \alpha_{y\theta} \\ \alpha_{\theta x} & \alpha_{\theta y} & \alpha_{\theta\theta} \end{bmatrix} \begin{bmatrix} F_x \\ F_y \\ M_\theta \end{bmatrix} \tag{3.35}$$

To find α_{xy}, we first find the 3-DOF stiffness matrix for a single U-spring:

$$\begin{bmatrix} F_x \\ F_y \\ M_\theta \end{bmatrix} = \begin{bmatrix} k_{xx} & k_{xy} & k_{x\theta} \\ k_{yx} & k_{yy} & k_{y\theta} \\ k_{\theta x} & k_{\theta y} & k_{\theta\theta} \end{bmatrix} \begin{bmatrix} x \\ y \\ \theta \end{bmatrix} \tag{3.36}$$

In section 3.2.1, we used energy methods to find the spring constants k_{xx}, k_{yy}, $k_{\theta\theta}$. We apply the same method to find the cross-coupled stiffness coefficients, k_{xy}, $k_{y\theta}$, $k_{x\theta}$. for the single U-spring, using appropriate boundary conditions. Then we add together the four stiffness matrices of the four U-springs, considering the changing direction of local coordinates. The last step is to obtain the compliance matrix as shown in equation (3.35) by inverting the total stiffness matrix. The result shows that both the stiffness and the compliance matrix are symmetric, as expected.

The full formula for α_{xy} is extremely long and can not be listed here. For most designs, the four U-spring beams and trusses are designed with the same length and width. If there are no process variations, the spring beams are perfectly matched. In this case, the stiffness matrix and compliance matrix are both diagonal, $\alpha_{xy} = 0$ and there is no cross-axis sensitivity.

However, in actual fabrication, process variations will cause mismatch of the spring beams, predominantly of the beam widths. In this case, α_{xy} is not equal to zero and the acceleration in the y-direction will produce a non-zero output voltage.

The cross-axis sensitivity of an accelerometer is formulated as the ratio of voltage output due to orthogonal axis acceleration (y-axis) over the voltage output due to the same amount of acceleration in the

primary axis (x-axis) [6]:

$$S_{cr} = \frac{m_{y,\,eff} a \alpha_{xy}}{(m_{x,\,eff} a)/k_{xx}} = k_{xx}\alpha_{xy}\left(\frac{m_{y,\,eff}}{m_{x,\,eff}}\right) \tag{3.37}$$

where $m_{y,eff}$ and $m_{x,eff}$ are the effective mass in the y and x directions, respectively. In most cases, $m_{y,\,eff} \approx m_{x,\,eff}$, and $S_{cr} \cong k_{xx}\alpha_{xy}$. We compare our cross-axis sensitivity model with finite element simulation results in Section 5.3.

3.3.5 Mechanical bandwidth

From equation (3.21), letting $s = j\omega$, the amplitude is

$$\frac{|X(j\omega)|}{|A(j\omega)|} = \frac{1}{\sqrt{\left(\omega_r^2 - \omega^2\right)^2 + \left(\frac{\omega_r \omega}{Q}\right)^2}} \tag{3.38}$$

We define the mechanical bandwidth of the accelerometer as the -3dB cut-off frequency, where $\left|X(j\omega_{-3dB})\right| = |X(0)|/\sqrt{2}$.

$$\omega_{-3dB} = \omega_r \sqrt{1 - \frac{1}{2Q^2} + \frac{1}{2Q^2}\sqrt{1 - 4Q^2 + 8Q^4}} \tag{3.39}$$

where ω_r is the resonant frequency, Q is the quality factor.

3.4 Force-feedback control for accelerometer

3.4.1 Feedback system formulation

Closed-loop operation can improve the performance of the accelerometer in several ways. It increases the maximum detectable acceleration by providing feedback force against large accelerations. Sensitivity and bandwidth can be made independent from their mechanical values, and can be controlled by the feedback loop. The control can be implemented with either analog feedback [6] or a digital sigma-delta (ΣΔ) approach [12]. Details of different circuit implementations for the feedback loop are beyond the scope of our layout synthesis and will not be discussed. However, we model an analog feedback system at a generic conceptual level to include closed-loop effects in our synthesis.

A schematic of the feedback system is shown in Figure 10. The feedback system consists of a mass-spring-damper system representing the mechanical part of the accelerometer, a position sensor representing the capacitive sensing interface, a proportional plus derivative compensator and a force transducer. The compensator $G_0 + G_1 s$ is basically a lead filter to increase the stability of the system by putting a left-plane zero into the loop gain. The force transducer has a linear force-voltage relation of equation (3.18), $K_F = 2V_{C,dr}C_F/g_f$. From discussions in Section 3.3.1, the coefficient of the position sensor $K_V = (V_m/g_0)2C_0/(2C_0 + C_{para})$. Compensator coefficients G_0 and G_1 need to be found for the feedback system.

From Figure 10, the closed-loop transfer function is

$$H(s) = \frac{V_{out}(s)}{F_{in}(s)} = \frac{K_V}{ms^2 + (B + G_1 K_F K_V)s + (K_F K_V G_0 + k)} \tag{3.40}$$

The steady-state value of $V_{out}(t)$ can be found by the final-value theorem [19]:

$$\lim_{t \to \infty} V_{out}(t) = \lim_{s \to 0} s\left(\frac{V_{out}(s)}{s}\right) = \frac{K_V}{K_F K_V G_0 + k} F_{in} \tag{3.41}$$

The steady-state value of the displacement $x_o(t)$ for an input acceleration a_{in} is:

$$x_{o,steady} = \lim_{t \to \infty} \frac{V_{out}(t)}{K_V} = \frac{ma_{in}}{K_F K_V G_0 + k} \tag{3.42}$$

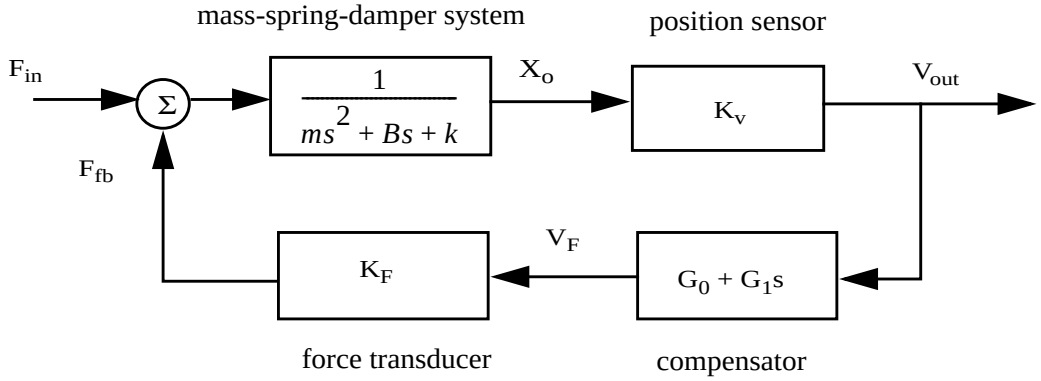

Figure 10. Analog feedback loop

G_0 and G_1 are determined by two equations. The first one comes from the system stability requirement. By letting the second-order system critically damped, we have

$$(B + G_1 K_F K_V)^2 = 4m(K_F K_V G_0 + k) \tag{3.43}$$

The second equation is obtained by setting $x_{o,steady}$ to some fixed value. Solving equation (3.42) and (3.43), we have G_0 and G_1 as

$$G_0 = \frac{ma_{in} - kx_{o,\,steady}}{K_F K_V x_{o,\,steady}} \qquad G_1 = \frac{-B + 2m\sqrt{\dfrac{a_{in}}{x_{o,\,steady}}}}{K_F K_V} \tag{3.44}$$

In our synthesis formulation, if the proof-mass displacement caused by user-specified maximum input acceleration $a_{max,spec}$, $x_{max,open} = ma_{max,spec}/k$, is less than the open-loop snap-in displacement x_{snap} discussed in Section 3.3.3, $x_{o,steady}$ is set to the $x_{max,open}$ because snap-in will not occur. In this case, there is no feedback force in steady state, i.e. the system is open-loop for the steady state. However, feedback force is required to meet an user-specified transient response. If $x_{max,open}$ is larger than x_{snap}, then $x_{o,steady}$ is set to x_{snap}. Figure 11 shows example step response waveforms of $x_o(t)$ and $F_{fb}(t)$ for open-loop and closed-loop operation.

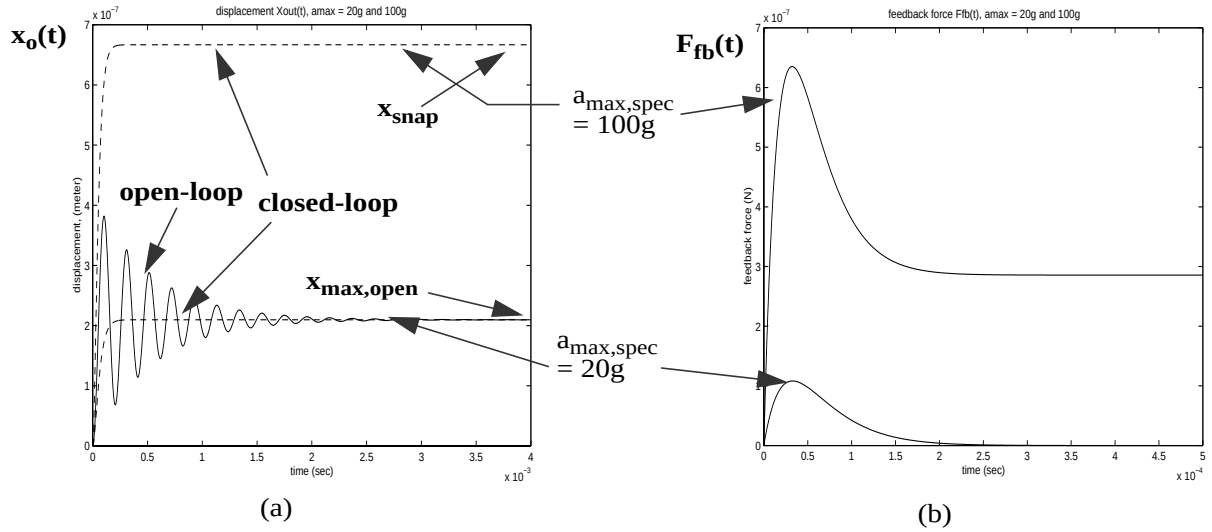

Figure 11. Step response of $x_o(t)$ and $F_{fb}(t)$ for specified $a_{max,spec} = 20g$ and $100g$. $F_{in} = ma_{max,spec}$. (a) open-loop $x_o(t)$ (solid line), closed-loop $x_o(t)$ (dotted line). (b) $F_{fb}(t)$ (solid line). There is no open-loop $x_o(t)$ waveform for $a_{max,spec} = 100g$ because of snap-in.

In both cases, the proof-mass displacement $x_o(t)$ in closed-loop operation are settling much faster than that in open-loop because of the lead compensation. In Figure 11(a), $x_{max,open}$ is smaller than x_{snap} because of the small a_{max} (20g) specification. There is no feedback force in steady state, but transient feedback force is needed if critical damping is specified. The closed-loop and open-loop displacement $x_o(t)$ settled at the same value $x_{max,open}$. In Figure 11(b), the large a_{max} (100g) specification requires feedback force even in steady state. The steady state closed-loop displacement $x_o(t)$ is $x_{snap.}$ Open-loop displacement is not shown because the snap-in will occur in this case since $x_{max,open} > x_{snap}$.

A critically damped closed-loop system increases a_{max} in two ways. First, it eliminates the displacement ringing so that the maximum displacement occurs only in the steady state. Second, a feedback force is provided to pull the proof-mass back in steady state when a large input acceleration is applied. We will discuss other device performance parameters affected by the feedback force in the following sections.

3.4.2 Accelerometer performance evaluation models in closed-loop

3.4.2.1 Sensitivity in closed-loop

From equation (3.41) and (3.44), the closed-loop sensitivity is obtained as:

$$\left(\frac{V_{out}}{a}\right)_{closed} = \frac{mK_V}{K_F K_V G_0 + k} = K_V \frac{x_{o,\,steady}}{a_{max,spec}} \tag{3.45}$$

When $x_{o,steady}$ is less than or equal to $x_{max,open}$, the closed-loop sensitivity is same as the open-loop sensitivity given by equation (3.26) because $\frac{x_{max,open}}{a_{max,spec}} = \frac{m}{k}$. In this case, there is no feedback force in the steady state. When $x_{o,steady}$ is equal to x_{snap}, the sensitivity can be set independently from its open-loop value because of the feedback force in steady state. Sensitivity will be specified as input to the synthesis, which will constrain values of $x_{o,steady}$ and G_0.

3.4.2.2 Minimum detectable acceleration in closed-loop

Since an ideal feedback network does not add noise into the system[12], the minimum detectable accel-

eration is given by same equation (3.29). But sensitivity used to refer circuit noise to the input in equation (3.28) is the closed-loop sensitivity.

3.4.2.3 Maximum detectable acceleration in closed-loop

As discussed in Section 3.4.1, the closed-loop improves the accelerometer range by reducing ringing during the settling time and providing feedback force in steady state. From Figure 10, the transfer function for the feedback force controlling voltage V_F is:

$$\frac{V_F(s)}{F_{in}(s)} = \frac{K_V(G_0 + G_1 s)}{ms^2 + (B + G_1 K_F K_V)s + (K_F K_V G_0 + k)} \tag{3.46}$$

By using Equation (3.43) and taking Laplace transform, its transient response to a step input a_{in}(t) is

$$V_F(t) = a_{in}(t)\frac{K_V}{\alpha^2}[G_0 - G_0 e^{-\alpha t} - \alpha(G_0 - \alpha G_1)te^{-\alpha t}] \tag{3.47}$$

where $\alpha = (B + G_1 K_F K_V)/2m$. It has a maximum $V_{F,peak}$ at

$$t_{peak} = \frac{G_1}{\alpha G_1 - G_0} \tag{3.48}$$

The appearance of a maximum $V_{F,peak}$ can be seen from Figure 11(b), since $V_F(t)$ has a same waveform shape as $F_{fb}(t)$.

As the input acceleration is increased, the controlling voltage V_F is increased to provide enough feedback force. The maximum detectable acceleration occurs when $V_{F,peak}$ reaches its largest available value $V_{F,max}$. From equation (3.47), we have

$$a_{max,closed} = \frac{V_{F,max}\alpha^2}{K_V}[G_0 - G_0 e^{-\alpha t_{peak}} - \alpha(G_0 - \alpha G_1)t_{peak}e^{-\alpha t_{peak}}]^{-1} \tag{3.49}$$

3.4.2.4 Cross-axis sensitivity in closed-loop

From the definition in Section 3.3.4, the cross-axis sensitivity in closed loop is

$$S_{cr,closed} = \frac{m_{y,eff}a\alpha_{xy}}{(m_{x,eff}a)/k_{xx}} = k_{xx}\alpha_{xy}\frac{m_{y,eff}}{m_{x,eff}} \tag{3.50}$$

which is the same as Equation (3.36) of the open loop operation.

3.4.2.5 Bandwidth of the close-loop system

From Figure 10, we can write the transfer function for the proof-mass displacement as

$$X(s) = \frac{mA(s)}{ms^2 + (B + G_1 K_F K_V)s + (K_F K_V G_0 + k)} \tag{3.51}$$

The resonant frequency $\omega_{r,close}$ is

$$\omega_{r,\,closed} = \sqrt{\frac{K_F K_V G_0 + k}{m}} = \sqrt{\frac{a_{max,spec}}{x_{o,\,steady}}} \tag{3.52}$$

Note again that, when $x_{o,steady} = x_{max,open}$, $\omega_{r,closed} = \omega_{r,open}$.

Also defining the close-loop bandwidth as the -3dB cut-off frequency as we did in open-loop, we have

$$\omega_{-3dB,closed} = \omega_{r,\,closed}\sqrt{1 - \frac{1}{2Q_{r,\,closed}^2} + \frac{1}{2Q_{r,\,closed}^2}\sqrt{1 - 4Q_{r,\,closed}^2 + 8Q_{r,\,closed}^4}} \tag{3.53}$$

where $Q_{r,\,closed} = \frac{\omega_{r,\,closed} m}{B + G_1 K_F K_V}$ is the closed-loop quality factor.

3.4.3 Issues in feedback control

In Section 3.3.1, we made an assumption that, for the capacitive sense interface, the displacement x caused by the input acceleration is much smaller than the initial finger gap, i.e. the proof mass is approximately centered during the sensing. This assumption is not valid when large input is applied. Using the exact value of C_1 and C_2 into Equation (3.23), we have:

$$V_0 = \frac{2C_0}{2C_0 + C_{para}} \frac{x}{g} V_m \left(\frac{1}{1 - \frac{C_{para}}{2C_0 + C_{para}} \left(\frac{x}{g}\right)^2} \right) \tag{3.54}$$

Applying the Taylor's series expansion to Equation (3.54) and letting $A = C_{para}/(2C_0 + C_{para})$, we find the position sensor coefficient,

$$K_V = \frac{V_0}{x} = \frac{2C_0}{2C_0 + C_{para}} \frac{V_m}{g} \left[1 + A\left(\frac{x}{g}\right)^2 + A^2\left(\frac{x}{g}\right)^4 + A^3\left(\frac{x}{g}\right)^6 + \ldots \right] \tag{3.55}$$

When x is not much smaller than g, the high-order $\frac{x}{g}$ terms cannot be neglected, and the position sensor is nonlinear. The large displacement will also affect the linearity of the mechanical springs. All of these effects will cause the sensitivity to be nonlinear.

To solve this problem, feedback control systems tend to be designed to null the proof-mass position when the signal is applied. This can be done by a digital approach [17]. In analog approach, the simple single-zero leading compensation we introduced reduces proof-mass displacement but does not completely null its position. A possible approach to nulling is to add an integrator into the feedback loop so that the deflection of the proof mass from the center point is integrated. In the frequency domain, this approach is equivalent to adding a pole at s = 0 in the s plane. Additional left-plane zeros must be included to provide phase leading compensation for stability.

IV. Synthesis methodology

In order to model our design problem as a formal numerical synthesis problem, we need to identify the design variables which represent our accelerometer topology. Then the design space is defined by setting maximum and minimum values for the design variables. Design constraints which come from manufacturability and user specifications are formulated to further limit the design space. The design variables must meet the constraints for the design to be acceptable. The next step is to define the objective functions which drive the synthesis tool toward the optimum design. We will discuss the synthesis methodology in detail in next several sections.

4.1 Design variables

There are seventeen design variables identified for the accelerometer design. The design variables are shown in Figure 12(a). Table 1 shows the definition of the variables and their maximum and minimum values which are usually set by the polysilicon fabrication process. Maximum beam lengths are set to 400 μm to prevent beam curling due to stress gradients in the polysilicon film and possible sticking and breakage during the wet etch [20]. The minimum beam lengths, widths and beam spaces are set by technology-

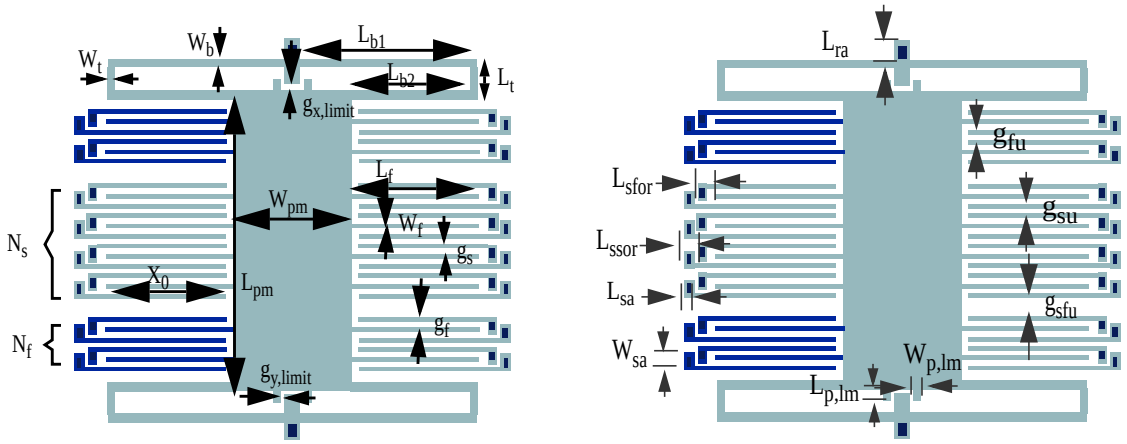

Figure 12. Design and style variables of accelerometers.
(a) Design variables (b) Style variables

driven design rules. Maximum beam widths are set to 20 μm by the limited undercut of silicon-oxide to release the structures. The maximum length of the proof mass is constrained to 700 μm by the size of the layout and the maximum width is constrained to 400 μm for the release of the mass. The minimum value of limit stop gap in x and y direction is set to 1μm. Although this gap size violates the design rules in some polysilicon process (*e.g.* MUMPs), the small gap is necessary to avoid fingers of different voltages from touching.

The style geometric variables are necessary to completely define the layout, but do not affect the performance of the accelerometer. The 10 style variables are shown in Figure 12(b) and also listed in Table1.

Table I Design and style variables for the accelerometer. Lengths and widths are in units of μm except *N* and *V*.

DESIGN VARIABLES							
Var.	**Description**	**Min**	**Max**	**Var.**	**Description**	**Min**	**Max**
L_{b1}	length of spring beam 1	2	400	g_s	gap between sense finger	2	20
L_{b2}	length of spring beam 2	2	400	g_f	gap between feedback finger	2	20
W_b	width of spring beam	2	20	X_0	comb finger overlap	2	400
L_t	length of truss beam	2	400	g_{xlim}	gap limit x displacement	1	20
w_t	width of truss beam	2	20	g_{ylim}	gap limit y displacement	1	20
L_{pm}	length of proof-mass	2	700	N_s	number of sense comb fingers	1	100
W_{pm}	width of proof-mass	2	400	N_f	number of feedback comb fingers	1	100
L_c	length of comb finger	2	400				
W_c	width of comb finger	2	20	V	voltage amplitude	1V	2.5V

STYLE VARIABLES							
g_{su}	gap between sense unit	2	2	L_{sa}	length of stator anchor	11	11
g_{fu}	gap between feedback unit	2	2	W_{sa}	width of stator anchor	11	11
g_{sfu}	gap of sense andfbk unit	10	10	$L_{p,lm}$	length of limit post	2	2
L_{sfor}	length of stator over rotor fgr	21	21	$W_{p,lm}$	width of limit post	2	2
L_{ssor}	length diff. of stator fingers	16	16	L_{ra}	spring anchor length	15	15

They define the stationary parts of the accelerometer, such as the gap between sensing and feedback units, the length of stator finger over rotor finger. These variables are set to fixed values, usually minimum values the fabrication process allowed to reduce the device size.

4.2 Design constraints

4.2.1 Geometrical constraints

Geometrical constraints are design constraints related to the layout dimensions and are necessary for a physically valid design. In our accelerometer design, we have 11 geometrical constraints as shown in Figure 13 and also listed in Table 2.

The first three constraints determine the size of the device. The length and width should not be over an arbitrary fixed size, 700 μm in our example. The width of the device could be the U-spring length or the

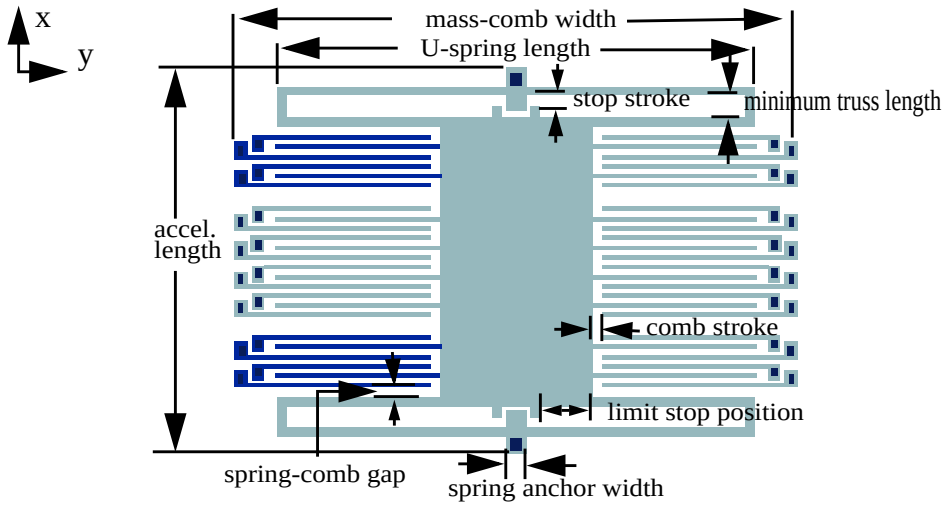

Figure 13. Geometric constraints of accelerometer layout

total mass-comb width, so both of them must less than 700 μm. The width of the spring anchor is calculated from L_{b1}, L_{b2} and W_{pm} and must be greater or equal to the minimum anchor width, 11 μm. To prevent fingers of different voltages from touching each other, the gap between sense fingers and feedback fingers must be larger than the limit-stop gap in x direction $g_{x,limit}$, and the comb stroke in y direction should be larger than $g_{y,limit}$. There is an additional constraint on L_{b1} and L_{b2} that ensures the limit-stop posts are attached to the proof mass instead of the spring beam. The gap between the limit stop and the spring should be larger than the minimum space 2.0 μm and constrains the minimum truss length. It also must be larger than $g_{x,limit}$ to make $g_{x,limit}$ an effective displacement limit in the x direction, which is called the stop stroke. All the above constraints are linear constraints. However, there is one nonlinear geometric constraint, the gap between the spring and comb finger.

Table 2: Geometric constraints

Constraint Description	Expression	min [μm]	max [μm]
accelerometer length	$L_{pm}+2(L_t+L_{ra})$	0	700
mass-comb width	$W_{pm}+2(L_c+2L_{sfor}+L_{ssor})$	0	700
spring length	$W_{pm}+2(L_{b2}+W_t)$	0	700
spring anchor width	$W_{pm}+2(L_{b2}-L_{b1})$	11	100
x displacement limit I	$g_s-g_{x,limit}$	0.2	20
x displacement limit II	$g_f-g_{x,limit}$	0.2	20
comb stroke	$L_c-X_0-g_{y,limit}$	2	20
limit stop position	$L_{b1}-L_{b2}-g_{y,limit}-W_{p,lm}$	0	400
minimum truss length	$L_t-W_b-L_{p,lm}$	2.0	400
stop stroke	$L_t-W_b-L_{p,lm}-g_{x,limit}$	0	400
spring-comb gap	$[L_{pm}-2W_b-2N_f(3W_c+2g_f)-2(N_f-1)g_{fu}-N_s(3W_c+2g_s)-(N_s-1)g_{su}-2g_{sf}]/2$	10	20

4.2.2 Functional constraints

In Section 3.3 and 3.4, we discussed models for the parameters used to specify the accelerometer performance. In order to synthesize a valid design, these specifications must be assigned realistic values, which are bounded by the functional constraints listed in Table 3.

The minimum sensitivity, maximum noise, minimum range and maximum cross-axis sensitivity are specified by users. The bandwidth could be the mechanical bandwidth in open-loop or loop bandwidth in close-loop. Resonant frequencies of other in-plane modes, f_x and f_θ, must be at least three times greater than f_x to decouple the modes adequately.

Table 3: Functional constraints

Constraint Description	Expression	min	max
Sensitivity	$S = V_o/a_{in}$	S_{spec}	1000 mv/g
Noise (min detectable accel.)	a_{min}	0.0 mg	$a_{min,\ spec}$
Range (max detectable accel.)	a_{max}	$a_{max,\ spec}$	10^4 g
Cross-axis sensitivity	S_{cr}	0.0	$S_{cr,spec}$
Bandwidth	ω_{-3dB}	$\omega_{-3dB,\ spec}$	10^5 Hz
Spring softening	$k_{x,elec}/k_{x,mech}$	0	0.9
Self_test force	test_force/(mx*range*9.8)	0.2	10^3
In-plane mode separation	f_x/f_y, f_x/f_θ	0	1/3
Beam buckling	L_b/L_{cr}	0	1/2

As we discussed in Section 3.2.5, the modulation voltage V_m will cause an equivalent electrical spring, $k_{x,elec}$. Its reaction force acts in the opposite direction of the mechanical spring, $k_{x,mech}$. When it is greater or equal to $k_{x,mech}$, the sense fingers will snap in for a very small input or even no input. Obviously, it is not a valid design. So we need to constrain that $k_e < 0.9k_{mech}$. Another constraint is added to generate enough self-test electrostatic force. In our synthesis, we want to generate a self-test force equivalent to 20% of the maximum detectable acceleration force [6].

In the fabrication process of the accelerometer, deposition of the structural material (usually polysilicon) will cause either compressive or tensile stress in the film. The stress will cause released beams to break in tension or buckle under compression. For example, in the MUMPs process, polysilicon beams have a compressive residual stress with a nominal value of -10 MPa. In the case of the U-spring, beams are free to expand outward to relieve residual axial stress. But the expansion of the proof mass will create additional axial stress in the inner beam (beam 2) and tension in outer beam (beam 1). A first-order value of the

critical buckling length, L_{cr} is given by the Euler column formula, $L_{cr} = \pi t\sqrt{2L_b/3\Delta}$, where t is the minimum of the width and thickness of the beam, Δ is the expansion length of the proof mass and calculated by $\Delta = W_{pm}\sigma_r E$, where σ_r is the residual and E is the Young's modulus. To ensure no buckling, the constraint $2L_b < L_{cr}$ is added.

4.3 Synthesis algorithm

In accelerometer synthesis, several designs or no designs may satisfy the constraints. We select the design which minimizes an objective function, and may be considered optimal. Usually, devices of smaller area are preferred for low cost. Also accelerometers with low noise (minimum detectable acceleration) are preferred for their ability to detect very small signals. And there are situations in which high-G accelerometers are needed, for example, accelerometers used for shock and impact measurement. So we choose four possible objective functions: minimize total area, minimize noise, minimize the sum of noise and area normalized to the maximum possible area and noise, and maximize detectable range (maximum detectable acceleration). Sensitivity is also a very important specification, but it can be easily increased by the amplifying circuit after the capacitive sense interface, so we did not list it as an objective function.

The synthesis problem is mapped onto a constrained optimization formulation that is solved using a nonlinear constrained optimization technique. During the optimization, designs defined by lumped-parameter macromodels are evaluated by the values of the constraints and the objective functions. Due to the complex nonlinear characteristics of the equations in the lumped-element macromodel, there can be more than one minimum point in the optimization for different objective functions. To perform synthesis in the entire design space, our tool should be independent of any choice of the starting point.

To solve for the global minimum of the objective function, we used a gridded multi-start algorithm coupled with a gradient-based constrained optimization (NPSOL) [21]. The use of a starting grid eliminates the need to provide good starting points to the gradient-based optimization. The starting grid is gen-

erated by assigning 3 values (low bound, up bound and middle value) to each of the 17 design variables, leading to 3^{17} starting points. Each of these points in the design space is evaluated and 100 designs which best meet the constraints are stored. These 100 points are then used as the starting points for the gradient-based optimization and a final design is chosen from the 100 optimization runs by comparing the constraints and objective function.

The nonlinear constrained optimization formulation can be written as:

$$\min_{\underline{u}} \quad z = \sum_{i=1}^{k} w_i \bullet f_i(\underline{u})$$

$$s\dot{t} \qquad \underline{h}(\underline{u}) = 0 \qquad \underline{g}(\underline{u}) \le 0 \qquad \underline{u} \in U_P$$

where $\underline{u}$ is the vector of independent design variables given in Table 1; $f(\underline{u})$ is a set of objective functions; w_i is the scalar weights to balance competing objectives. $\underline{h}(\underline{u}) = 0$ and $\underline{g}(\underline{u}) \le 0$ are each a set of functions that implement the geometric and functional constraints given in Table 2 and Table 3, and U_p is the set of allowable values of $\underline{u}$ (described by the bounds in Table 1).

In our synthesis, some of the design variables (such as the number of comb fingers) are integer in nature. So we cannot completely model the design problem in the nonlinear constrained optimization formulation, which uses real numbers. We use a branch-and-bound algorithm to overcome this. Initially, a *relaxed* optimization which treats the number of comb fingers as continuous variables is run. Then the number of comb fingers are truncated to the nearest integer and removed from the list of design variables. The final synthesis design is obtained by running a *non-relaxed* optimization with the result of the *relaxed* problem as the starting point. In addition, all the geometry parameters in the physical design should be represented as integers with centi-micron units to describe a valid layout. After *non-relaxed* optimization, the values of the design variables are rounded off to the nearest centi-micron units.

4.4 Layout generation

After a set of optimized design variable values are obtained from the synthesis, a parameterized layout

generation tool, CAMEL[1] is used to generate a CIF file which contains the mask information required for fabrication of the accelerometer. The original version of CAMEL was extended to include modules for U-spring, differential comb finger and proof-mass layout generation.

V. Synthesis results and verification

The synthesis tool is used to generate layouts for both open-loop and closed-loop control. In this section, we present the layouts generated for different objective functions and discuss design trade-offs between these objective functions. The accuracy of the lumped-models used in the synthesis is evaluated by comparing the predicted values with finite-element simulation results.

5.1 Synthesis results for open-loop operation

Four sets of accelerometer layouts are synthesized for four different objective functions: noise, area, noise plus area, and range, as shown in Figure 14. Sensitivity of 5, 10, 20 and 30 mV/g are used as the input sensitivity specification.

When minimizing area is the objective function and the sensitivity specification increases, the number of sense fingers increase from 4 to 24 as shown in Figure 14(a). This increases the sensing capacitance and the effective mass. It also reduces the effective spring constant because of the increase of electrostatic force. All these facts effectively increase the sensitivity. However, the increase of comb fingers also causes an increase in device area, so there is a trade-off between the sensitivity and the area as shown in Figure 15(a), corresponding to the layouts in Figure 14(a). Noise and range specifications are set to 0.1 $mg/\sqrt{Hz}$ and 10 g respectively for this case. Accelerometer designers usually want to use many sense fingers and a large mass to increase the sensitivity when the fabrication process allows.

The layouts in Figure 14(b) are generated for minimize noise. All the devices have the maximum allowed dimension, 700 μm each side. The large area has several effects on the noise. First, it increases the effective mass which will reduce the Brownian noise (see Equation (3.27)). Second, the mass increase will

increase the sensitivity which will reduce the input-referred circuit noise (see Equation (3.28)) if the circuit noise is fixed. Third, the increase of area also increases the air damping. To a first-order approximation, the effective mass and the Couette and Strokes damping coefficient increase linearly with area. The Hagen-Poiseuille damping coefficient is a function of the structure thickness, the finger gap, the finger overlap and number of the fingers. It is not a direct function of the area. The number of fingers will not increase with the area when the finger width and gap is made larger. From Equation (3.27), the Brownian noise is proportional to the square root of the damping coefficient and inversely proportional to the effective mass, so the net result is that noise will be reduced by the large area.

There is a trade-off between the sensitivity and the noise because both Hagen-Poiseuille damping and the sensitivity change with the finger gap g_s, the finger overlap X_0 and number of sense fingers N_s. Figure 15(b) shows the change of the minimum noise with the sensitivity specification, corresponding to the layouts in Figure 14(b). The range specification is set to 10 g for this case. As the sensitivity specification increases, we see that the minimum noise increases. To minimize noise while meeting the sensitivity constraint, trade-offs are made among g_s, X_0 and N_s. In sensitivity of 5 and 10 mv/g case, the width and length of the proof mass are at their upper limit. This leads to maximum effective mass while keeping the finger overlap X_0 small to reduce the damping. The widths of the comb fingers in all four cases are substantially larger than the minimum value to increase the mass while keeping N_s small. The sense gaps g_s for sensitivity of 5, 10, 20 mv/g are also not at their minimum value to reduce the damping.

The minimize-area-and-noise layouts in Figure 14(c) are larger in size than the minimize-area layouts and smaller in size than the minimize-noise ones, as expected. The device area increases as the sensitivity specification increases, because both small noise and large sensitivity demand large area. The noise and range specifications are set to 0.1 $mg/\sqrt{Hz}$ and 10 g respectively.

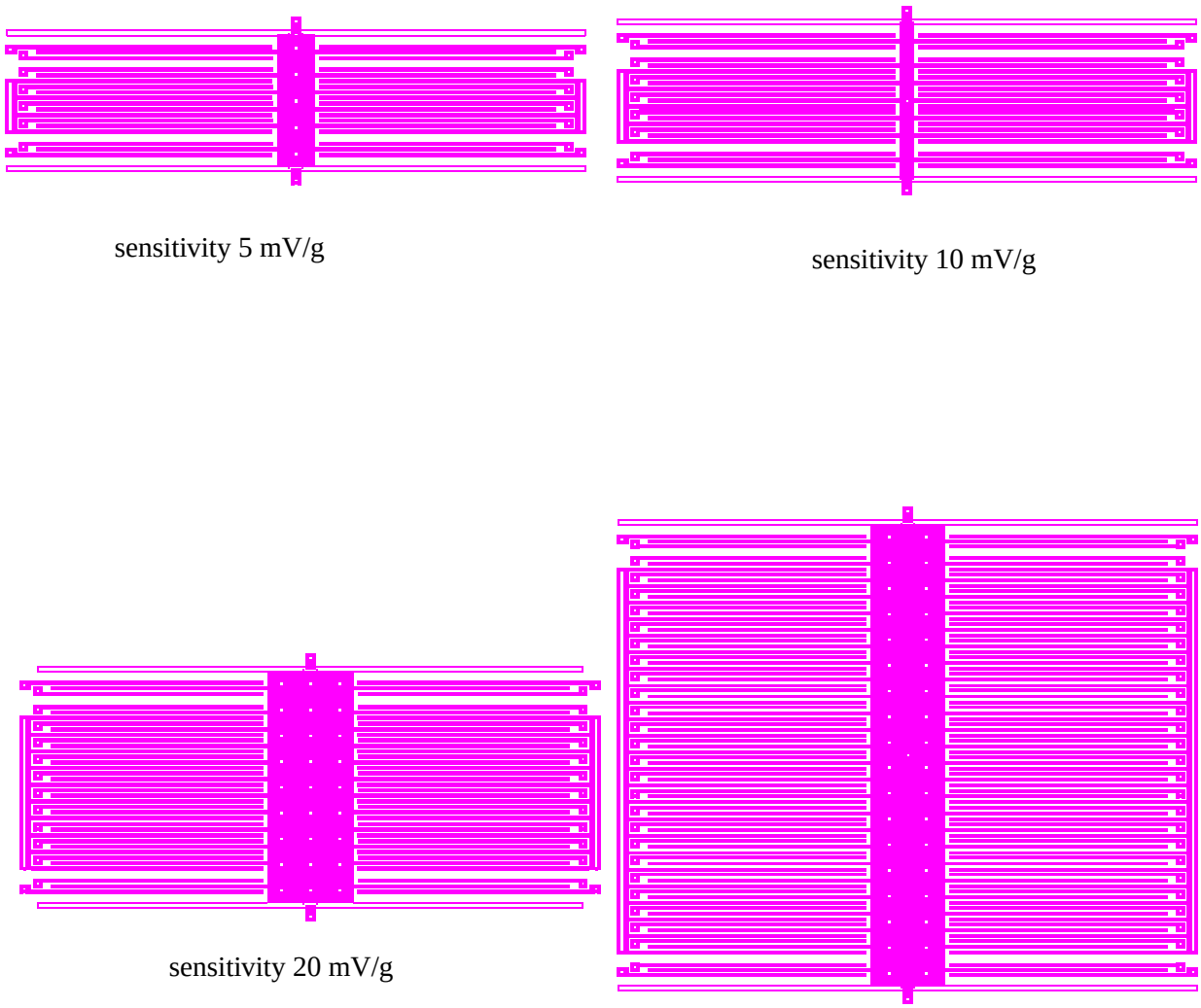

Figure 14(a). Synthesized accelerometer layouts for minimize-area with 4 sensitivity specs in open-loop operation.

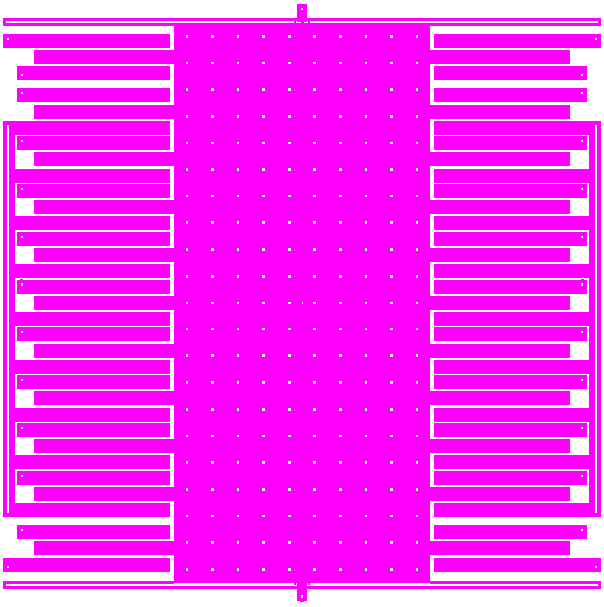

sensitivity 5 mV/g

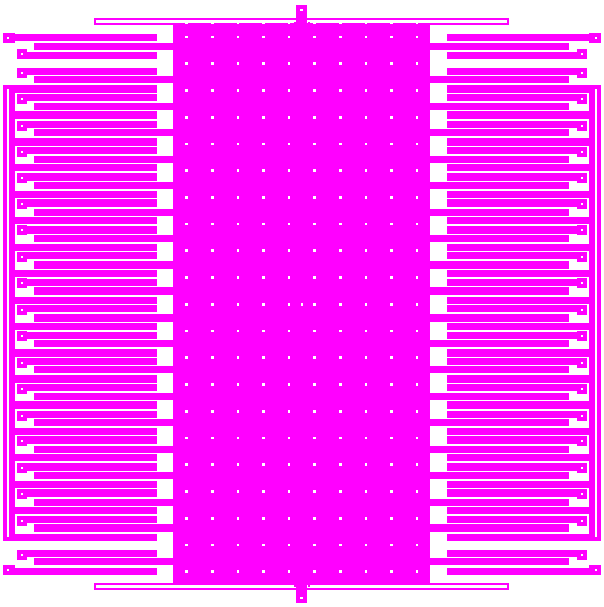

sensitivity 10 mV/g

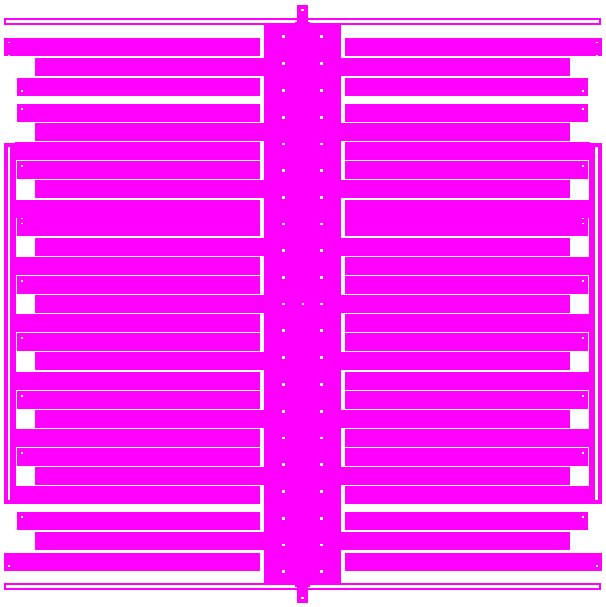

sensitivity 20 mV/g

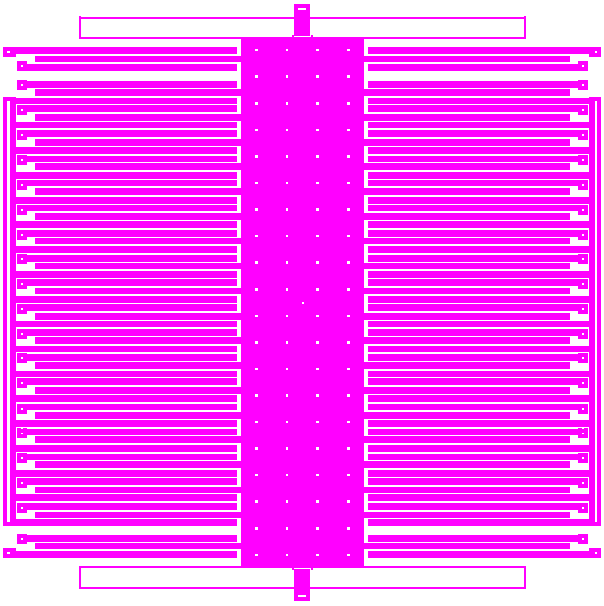

sensitivity 30 mV/g

Figure 14(b). Synthesized accelerometer layouts for minimize-noise with 4 sensitivity specs in open-loop operation.

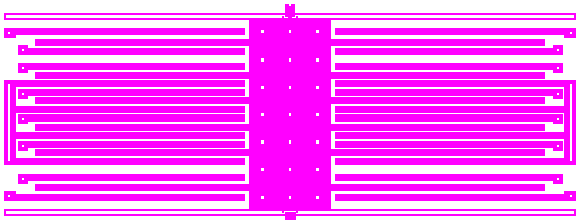

sensitivity 5 mV/g

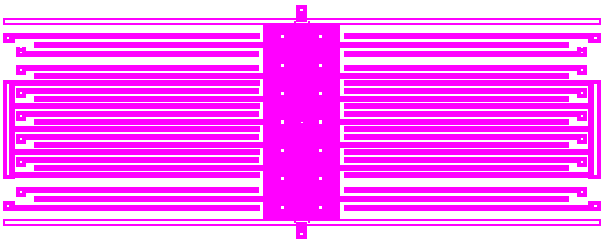

sensitivity 10 mV/g

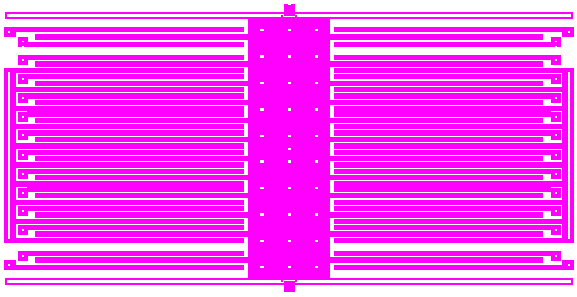

sensitivity 20 mV/g

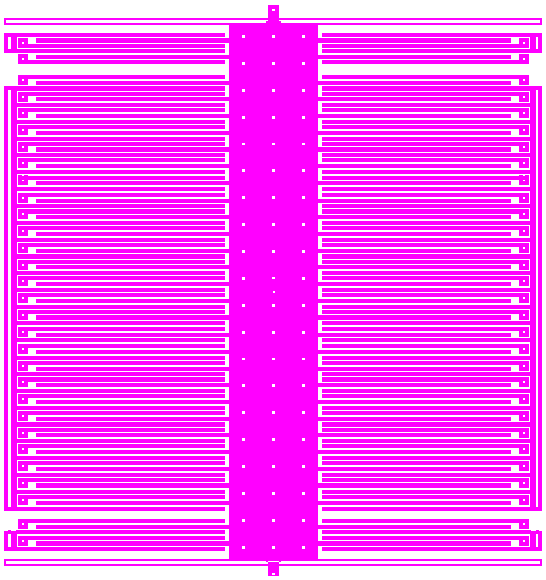

sensitivity 30 mV/g

Figure 14(c). Synthesized accelerometer layouts for minimize-area-and-noise with 4 sensitivity specs in open-loop operation.

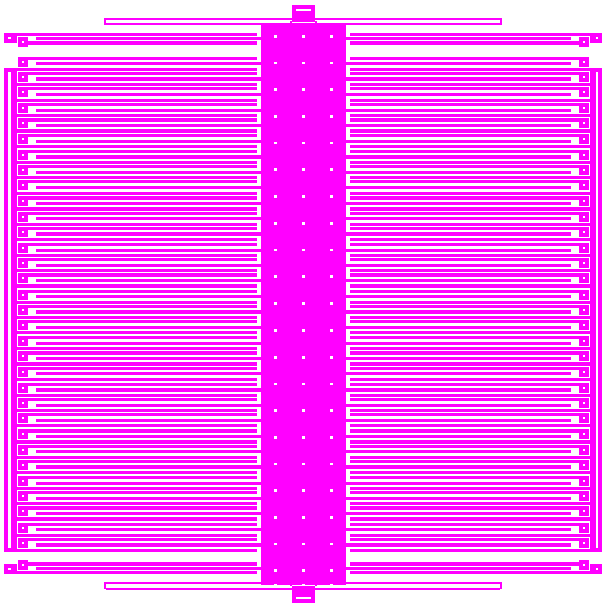

sensitivity 5 mV/g

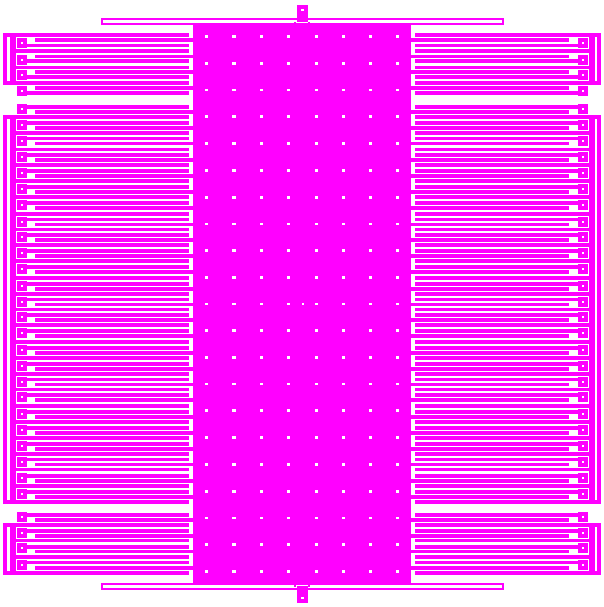

sensitivity 10 mV/g

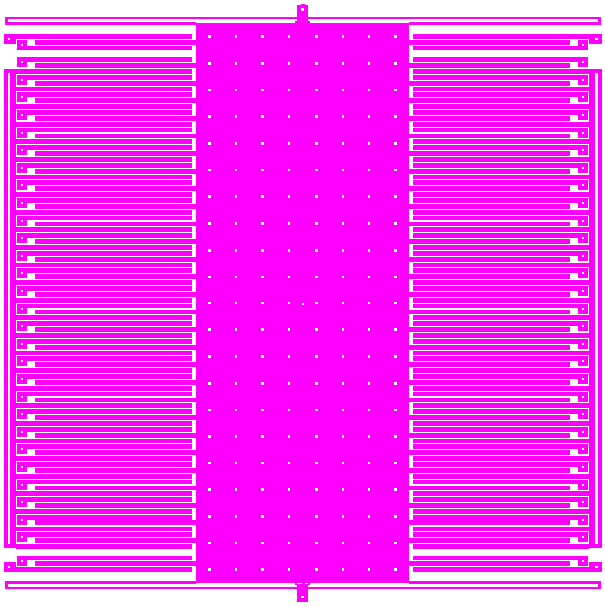

sensitivity 20 mV/g

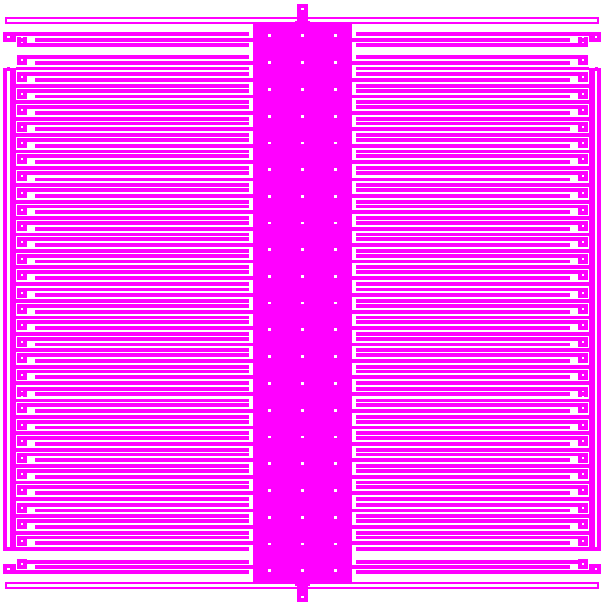

sensitivity 30 mV/g

Figure 14(d). Synthesized accelerometer layouts for maximize-range with 4 sensitivity specs in open-loop operation.

The maximize-range layouts shown in Figure 14(d) all have the maximum dimensions too. In open-loop operation, the range of the accelerometer increases quickly with the sense finger gap because of the quadratic relation between the electrostatic force and the gap width. To maximize range in small sensitivity, the gap is made larger than the minimum value. To maintain the required sensitivity, more sense finger and mass are needed. This leads to the large area. For large sensitivity specifications, large number of comb fingers, small gap and large sense finger overlap are needed. All these facts increase the electrostatic force and reduce the range. So there is also a trade-off between maximize-range and maximize-sensitivity as shown in Figure 15(c), corresponding to the layouts in Figure 14(d).

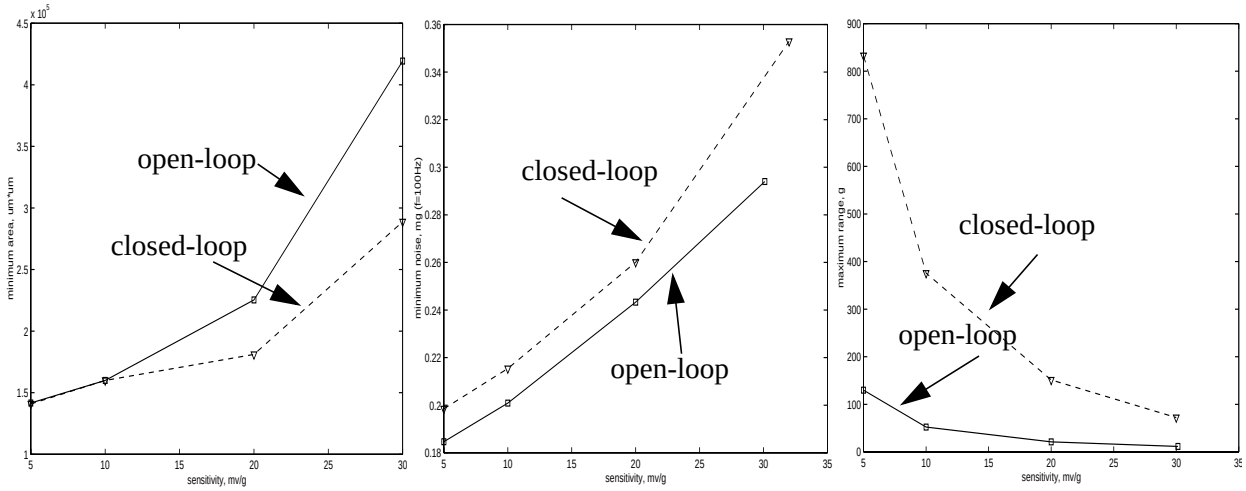

(a) (b) (c)

Figure 15. The change of minimum area, noise and maximum range with the sensitivity specifications. (a)minimum area vs. sensitivity specs (b)minimum noise vs. sensitivity specs (c) maximum range vs. sensitivity specs

5.2 **Synthesis results for closed-loop operation**

The same four objective functions and four sensitivity specifications are used to generate layouts shown in Figure 16 for closed-loop operation. The relations between minimum area, noise, maximum range and different sensitivity specifications in closed-loop are also shown in Figure 15 for comparison. The curves in Figure 15(a), (b) and (c) correspond to the layouts in Figure 16(a), (b) and (d) respectively.

In Figure 16(a), the noise and sensitivity specification are set to 0.1 $mg/\sqrt{Hz}$ and 10 g. Both open-loop and closed-loop cases have very small areas as shown in Figure 15(a). For small sensitivity, sensing

capacitance and mass required to meet the sensitivity are not at their maximum values, which makes the range specification easy to meet for both open-loop and closed-loop operation because large sensing capacitance and mass reduce the range. The small sensing capacitance and small number of feedback fingers (1 for both cases) also make the noise specification easy to meet. As the sensitivity specification increases, the number of sense fingers and mass are increased. In open-loop, more sense fingers are needed ($N_s=24$ for open-loop compared to $N_s=17$ for closed-loop for a sensitivity specification of 30 mV/g) for a required sensitivity because the gap of the sense fingers is made larger than the minimum value of 2 μm (3.2 μm for 30 mV/g sensitivity) to meet the range requirement. In closed-loop, the sense-finger gap can be set to its minimum value (2 μm for 30 mV/g sensitivity) and still meet the range specification because of the feedback force.

From Figure 15(b) we can see that the minimum noise of the closed-loop is larger than that of the open-loop in all four cases. For the small sensitivity case, this is mainly due to the increase in the number of force fingers. In open-loop, the force finger is only used to generate self-test force and the number of force fingers is one for all cases. While in closed-loop, the force finger is used to generate feedback force and the range specification constrains the number of force fingers. The number of force fingers for sensitivity of 5 mv/g and 10 mv/g for closed-loop is 9 and 2 respectively. However an increase in the sensitivity specification requires more sense capacitance and leads to only one feedback finger for sensitivity of 20 mV/g and 30 mV/g in closed-loop. The larger noise for these two cases is due to the smaller finger gap and larger number of sense fingers which will increase the Hagen-Poiseuille damping. The range specification is set to 10 g.

In the maximize-range comparison shown in Figure 15(c), the ranges in closed-loop are much larger than those in open-loop, demonstrating the advantage of the force feedback. As the sensitivity specification gets larger, the maximum-range is also reduced because the number of sense fingers must be increased at the expense of a decrease in the number of feedback fingers numbers for a fixed device size. The number of

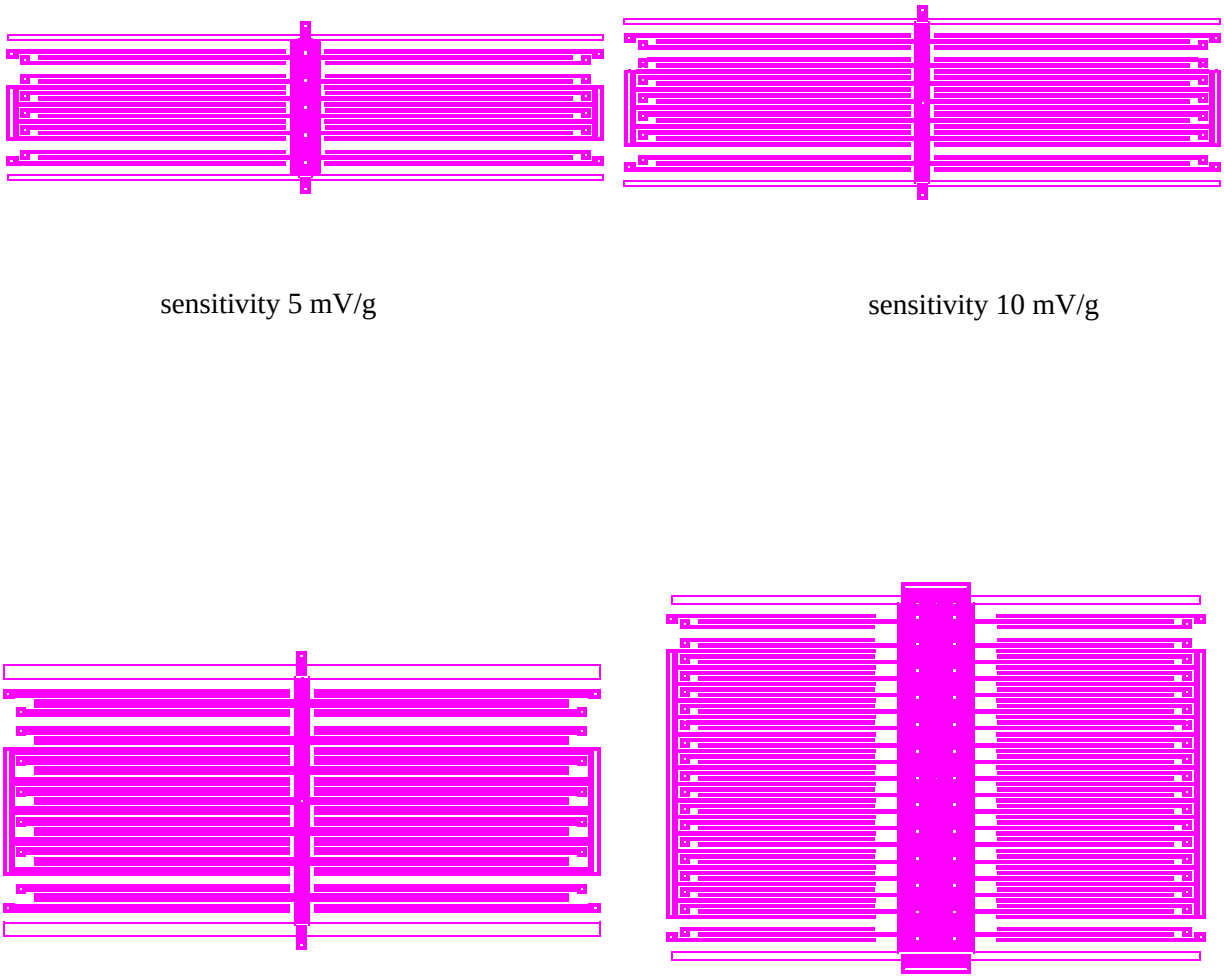

Figure 16(a). Synthesized accelerometer layouts for minimize-area with 4 sensitivity specs in closed-loop operation.

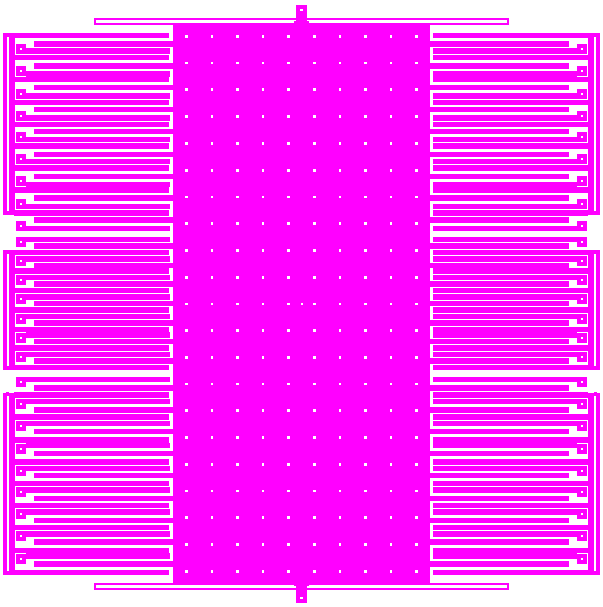

sensitivity 5 mV/g

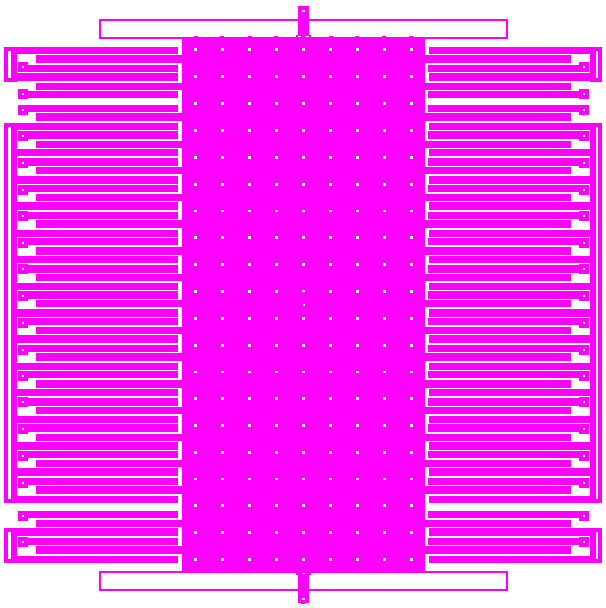

sensitivity 10 mV/g

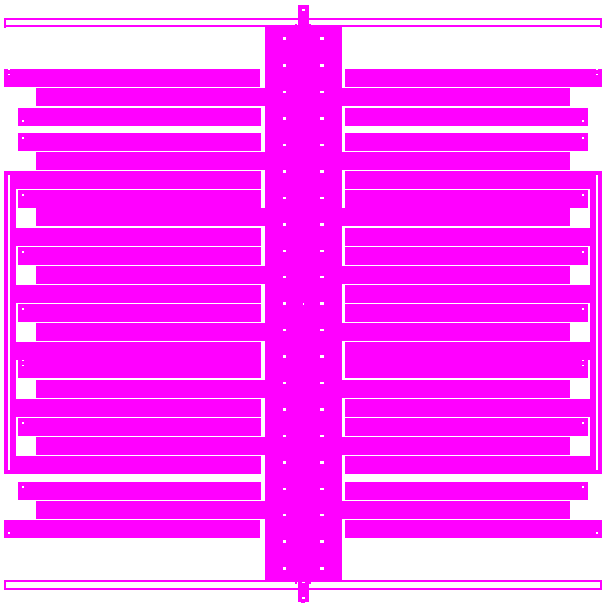

sensitivity 20 mV/g

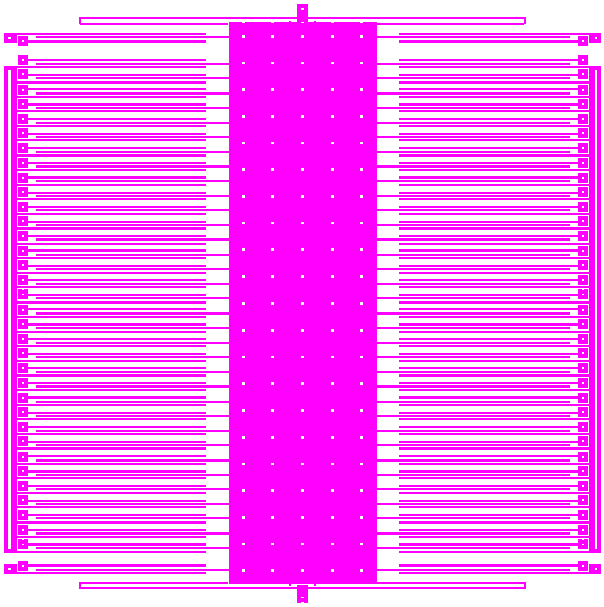

sensitivity 30 mV/g

Figure 16(b). Synthesized accelerometer layouts for minimize-noise with 4 sensitivity specs in closed-loop operation.

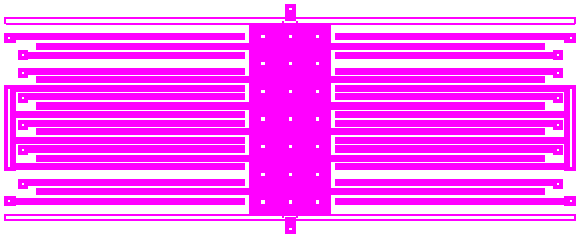

sensitivity 5 mV/g

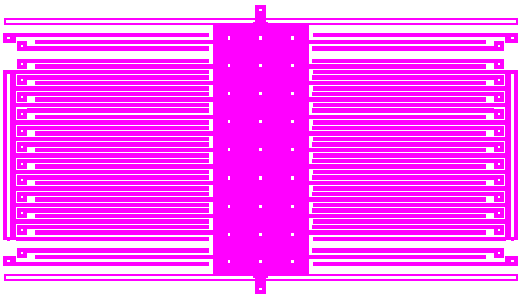

sensitivity 10 mV/g

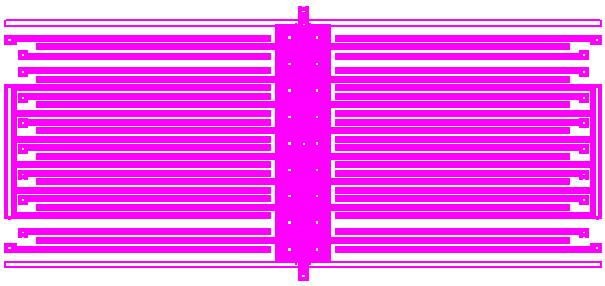

sensitivity 20 mV/g

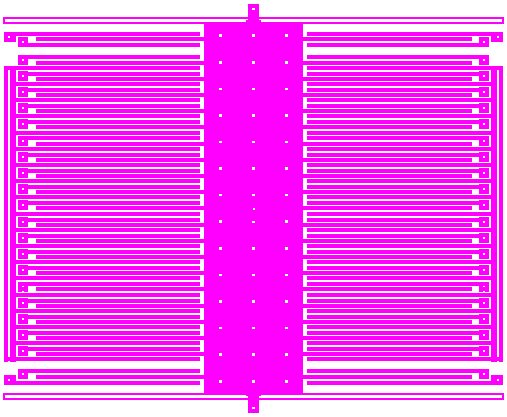

sensitivity 30 mV/g

Figure 16(c). Synthesized accelerometer layouts for minimize-area-and-noise with 4 sensitivity specs in closed-loop operation.

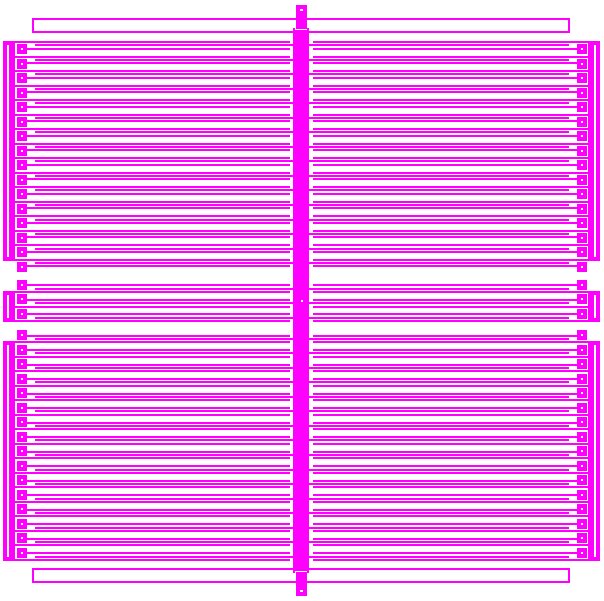

sensitivity 5 mV/g

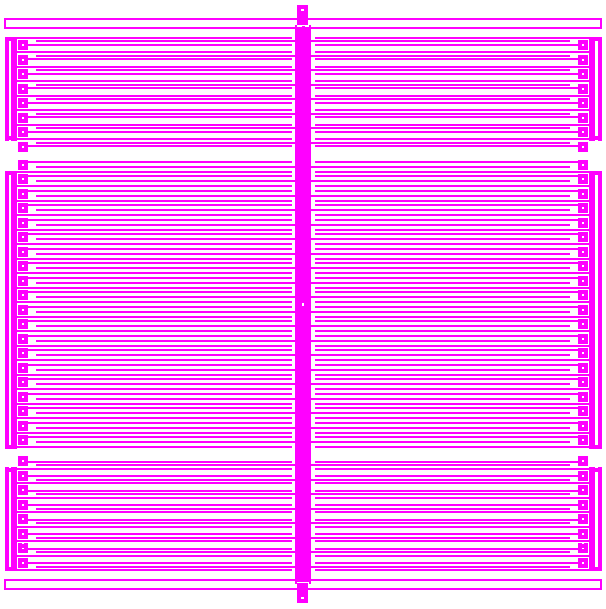

sensitivity 10 mV/g

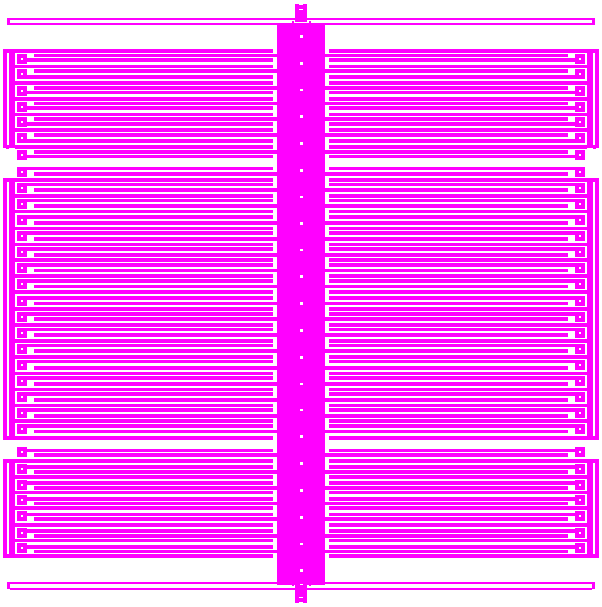

sensitivity 20 mV/g

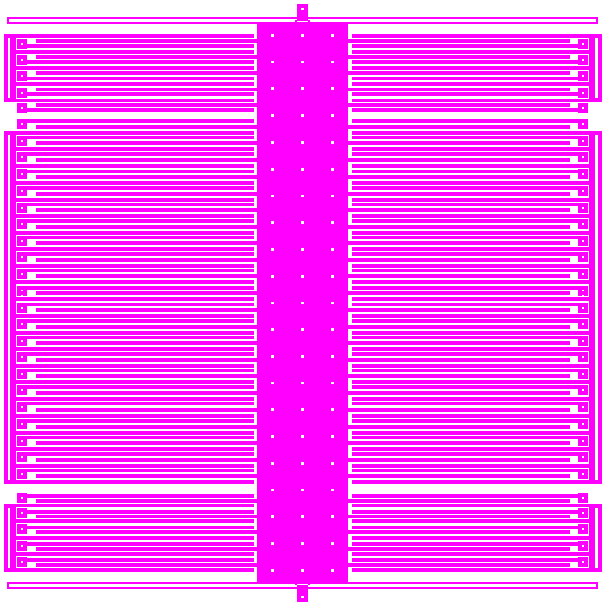

sensitivity 30 mV/g

Figure 16(d). Synthesized accelerometer layouts for maximize-range with 4 sensitivity specs in closed-loop operation.

feedback fingers are 16, 8, 7, 5 respectively for the four sensitivity specifications. The widths of the proof masses in Figure 16(d) are made small to allow large finger overlaps to generate large feedback forces. The noise specification is set to 0.1 $mg/\sqrt{Hz}$ for all four cases.

In conclusion, force feedback can increase the range of an accelerometer substantially and it also helps in reducing device area by allowing small sensing gaps. However, it increases the noise slightly even assuming no noise is added into the system by the feedback network. Whether an accelerometer should be designed as open-loop or closed-loop is a trade-off among accelerometer specifications such as range, noise, cost and linearity.

5.3 Finite element simulation verification

The finite-element analyses (FEA) tool ABAQUS [22] is used to verify the analytic expressions for mechanical spring stiffness, resonant frequencies and cross-axis sensitivity. In the simulation, 2D 8-node quadratic plane-stress elements are used to model the accelerometer structure. In Figure 17, the spring constants and resonant frequencies in *x*, *y* and θ directions from the FEA simulations are compared with our analytic models for the four designs in Figure 14(b). The analytical spring constants in x direction are within 7% of the FEA results. The x direction frequencies are within 5% of the FEA results which shows the accuracy of our effective mass models. The spring constants and frequencies in y direction (Figure 17(b)) are within 10%, 40% of the FEA results respectively. Predicted spring constants and resonant frequencies in θ direction have about 8%, 45% errors comparing with FEA results. So the primary x-mode which determines the mechanical sensitivity of the accelerometer is modeled within 7% accuracy, while other two modes are modeled within 45% accuracy. The large error for y and θ model occurs when the spring beam length is much larger than the truss length, for example, *Lb1* = 342.45μm and *Lt* = 6μm in sensitivity of 20 mV/g case. The error is mainly due to the effective mass model which does not include the spring velocity effects accurately.

We also verified the analytic model for the compliance coefficient α_{xy} used in cross-axis sensitivity calculation with FEA results, as shown in Figure 17(d). For the four different designs, the α_{xy} model is accurate to within 6%.

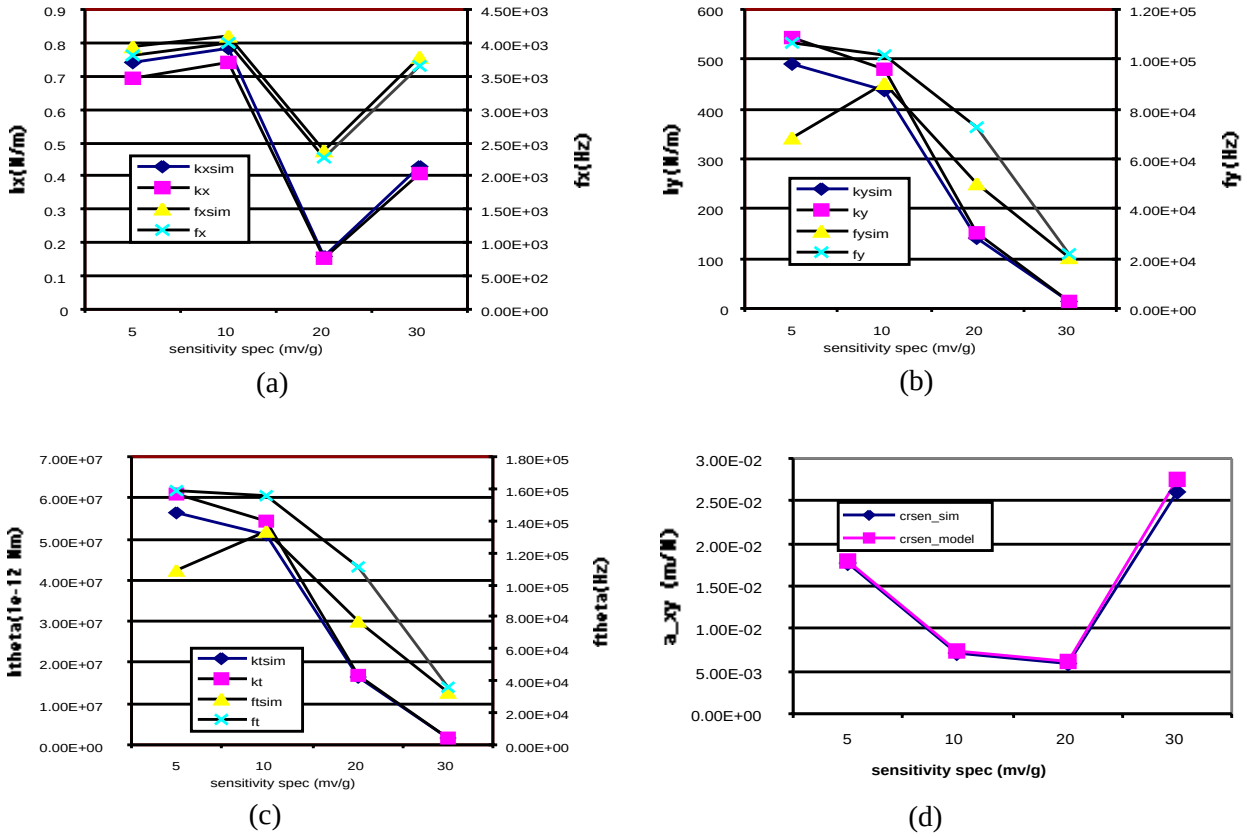

Figure 17. Comparison of predicted spring stiffness, resonant frequencies and compliance coefficient α_{xy} with finite-element simulation for the accelerometers shown in Figure 14(b). (a) spring constant and resonant frequency for x mode (b) spring constant and resonant frequency in y mode (c) spring constant and resonant frequency in θ mode (d) compliance coefficient α_{xy}.

VI. Conclusions and future work

This report describes a layout synthesis tool which can generate accelerometer layout from high-level specifications for different objective functions. An ADXL76 style accelerometer is chosen as the synthesis topology. Analytical models for spring constants, effective masses, air damping, electrostatic comb drive force are derived. A cross-axis sensitivity model which considers the manufacturing variation is also

derived. The results from finite-element simulation show that our analytical models for the spring constants, resonant frequencies in the primary x-direction and cross-coupled compliance coefficient are accurate to within 7%. A generic analog force-feedback loop is used to describe the closed-loop operation of the accelerometer. In the feedback loop, a simple phase-leading compensator is used to stabilize the accelerometer system. The analytic expressions for accelerometer performance evaluations are derived as functions of the lumped models for both open-loop and closed-loop operations. Layouts for different objective functions are generated. Trade-offs between different synthesis objectives are discussed based on the generated layouts. The synthesis results from open-loop operation and closed-loop operation are compared.

The synthesis work can be further investigated in several ways. The synthesized devices need to be manufactured by either MUMPs or iMEMS process and tested to verify and improve the analytical models. As stated in Section 3.4.3, a more sophisticated compensation scheme can be implemented for the force feedback to avoid the nonlinearity of system. Besides cross-axis sensitivity, more manufacturing variation issues need to be considered for accurate synthesis results, for example, incorporating the manufacturing variations into the spring stiffness, effective mass and air damping models. Another direction for the future work is to extend the synthesis methodology to any general MEMS device by automatic modeling and constraint generation from layout extraction.

VII. Acknowledgments

I would like to thank my advisor Prof. Gary Fedder and Dr. Tamal Mukherjee for their constant guidance, encouragement and support. I also thank Sitaraman Iyer, Gang Zhang, Mike Kranz, Xu Zhu, and rest of the MEMS group for helpful discussions. Finally, I would like to declare my deepest debt of gratitude to my wife, Yue, for her love and support for me all the time.

References

[1] Camel Web Page, http://www.mcnc.org/camel.org, MCNC MEMS Technology Applications Center, 3021 Cornwallis Road, Research Triangle Park, NC 27709.

[2] N. R. Lo, E. C. Berg, S.R. Quakkelaar, J. N. Simon, M. Tachiki, H. J. Lee, and K. S. J. Pister, "Parametrized layout synthesis, extraction, and SPICE simulation for MEMS", *Proc. ISCAS,* Atlanta, GA, 1996, pp. 481-484.

[3] D. Haronain, "Maximizing microelectromechanical sensor and actuator sensitivity by optimizing geometry", *Sensors and Actuators A*, 50(1995) , pp. 223-236.

[4] W. Ye, S. Mukherjee, and N.C. MacDonald, "Optimal Shape Design of an Electrostatic Comb Drive in Microelectromechanical Systems", *J. Microelectromechanical System,* March 1998, vol. 7, pp.16-26

[5] G.K. Fedder and T. Mukherjee, "Physical Design For Surface-Micromachined MEMS", *Proc. 5th ACM/SIGDA Physical Design* Workshop, Reston, VA, April 1996, pp.53-60.

[6] Analog Devices, "*ADXL150* - ±50 *g accelerometer with 10 mg resolution*", Datasheet, 1997, Norwood, MA 02062.

[7] *MUMPs Web Page*, http://mems.mcnc.org/mumps.html, MCNC MEMS Technology Applications Center, 3021 Cornwallis Road, Research Triangle Park, NC 27709.

[8] *iMEMS Web Page*, http://imems.mcnc.org/imems/imems.html, Analog Devices/MCNC, Analog Devices, One Technology Way, Norwood, MA 02062.

[9] J. M. Gere and S.P. Timoshenko, *Mechanics of Materials*, Chapter 7, pp. 412-413. Wadsworth, Belmont, 2nd ed., 1984.

[10] G. K. Fedder, *Simulation of Microelectromechanical Systems*, Ph.D. thesis, University of California at Berkeley, September 1994.

[11] Sitaraman Iyer, *Layout Synthesis of Microresonators*, M.S. Thesis, Carnegie Mellon University, May 1998, p9.

[12] M. A. Lemkin, *Micro Accelerometer Design with Digital Feedback Control*, Ph.D. thesis, University of California at Berkeley, August 1997.

[13] Y.-H. Cho, A.P.Pisano and R.T. Howe, *J. Microelectromechanical System,* vol. 3, (1994) pp. 81

[14] X. Zhang, W. C. Tang, "Viscous Air Damping in Laterally Driven Microresonators", *Sensors and Materials*, V. 7, no. 6, 1995, pp.415- 430.

[15] Yazdi, N., Najafi,K., "An all-silicon single-wafer fabrication technology for precision microaccelerometers", *The 9th International Conference on Solid-State Sensors and Actuators* - Transducers, '97, Chicago, Illinois, June 1997, pp.1181- 4.

[16] V.M. McNeil, M.J. Schmidt, MA, "Design and fabrication of thin-film microaccelerometers using wafer bonding", *The 7th International Conference on Solid-State Sensors and Actuators-Transducers*, '93, Yokohama, Japan, pp.822-25, June 1993.

[17] Boser B.E., Howe R.T., "Surface micromachined accelerometers", *IEEE Custom Integrated Circuits Conference*, 1995, pp. 337-344.

[18] N.R. Swart, S.F. Bart, M.H.Zaman, M. Mariappan, I.R. Gilbert, D. Murphy, "AutoMM: Automatic generation of dynamic macromodels for MEMS device", *Proceedings IEEE 11th Annual International Workshop on Micro Electro Mechanical System*, Heidelberg, Germany, January, 1998, p.178 - 183.

[19] G.F. Franklin, J.D. Powell, A.E. Naeini, *Feedback control of dynamic system*, Addison-Wesley, 1986, pp.547.

[20]C.H. Mastrangelo and C.H. Hsu, “A simple experimental technique for the measurement of the work of adhesion of microstructures”, *Technical Digest, IEEE Solid-State Sensor and Actuator Workshop*, Hilton Head Island, South Carolina, June 1992, pp.208-212.

[21]P.E.Gill, W.Murry, M.A. Saunders and M.H. Wright, User’s Guide for NPSOL (Version 4.0): A Fortran Package for Nonlinear Programming, Technical Report SOL 86-2, Stanford University, January 1986.

[22]*Abaqus User’s Manual, Version 5.6,* Hibbitt, Karlsson, and Sorensen, Inc., 1080 Main Street, Pawtucket, RI 02860.